UNIVERSITY OF GRONINGEN

MASTER'S THESIS

Specific mass and radial growth rates of galaxy disks at $z \simeq 1$

Author:
Thijs LUGGENHORST

Supervisors:
Prof. dr. Filippo FRATERNALI
Dr. Gabriele PEZZULLI
2nd Examiner:
Prof. dr. Reynier PELETIER

Kapteyn Astronomical Institute

Friday 9th July, 2021

ABSTRACT

Star-forming galaxies are predicted to grow their stellar mass inside-out, so that their size is expected to increase with time. In order to quantitatively test this theoretical prediction, Pezzulli et al. (2015) introduced a method which infers specific mass and radial growth rates (ν_M and ν_R, respectively) of galaxies by fitting star formation rate surface density (SFRD) profiles. However, this technique has only been applied to galaxies at $z \simeq 0$ so far. In this thesis we aim to quantify the growth of galaxies at $z \simeq 1$ by applying the SFRD fitting method from Pezzulli et al. (2015). We adopt a sample of 12 star-forming galaxies (of which 10 are included in our final analysis) from the KMOS Redshift One Spectroscopic Survey (KROSS) (Stott et al., 2016) at $z \simeq 1$, which was previously studied by Di Teodoro et al. (2016) and Marasco et al. (2019). Maps of Hα emission are extracted from KROSS data cubes for each galaxy, which are used as a tracer of the SFRD in our sample. We develop a fitting routine and test it by comparing inferred scale lengths of a sample of three galaxies from the KMOS^{3D} survey (Wisnioski et al., 2019) with findings by Wilman et al. (2020). We conclude that our fitting routine is robust as we find results that are in agreement with Wilman et al. (2020). We then proceed to use our routine to estimate the specific growth rates in our 10 galaxies. We find that the specific mass growth rates of our sample are in agreement with findings for the star formation main sequence relation at $z \simeq 1$ in the corresponding stellar mass range, found by Elbaz et al. (2007). 8/10 galaxies in our sample show positive radial growth rates, and only two show negative radial growth rates. We conclude that our results are consistent with the general picture of inside-out growth occurring at $z \simeq 1$. With a median ν_M of $0.763\,\mathrm{Gyr}^{-1}$ and median ν_R of $0.109\,\mathrm{Gyr}^{-1}$ we find that galaxies at $z \simeq 1$ grow ~ 7.5 times faster in mass and ~ 7 times faster in radius than their Local Universe counterparts. These results are in agreement with the main sequence of star formation. Furthermore, our results seem to be consistent with a model in which the mass-size relation is not strongly evolving with time.

Contents

Chapter 1

Introduction

1.1 Galaxy formation

One of the key ingredients in our theoretical understanding of the Universe is galaxy formation and evolution. This field, combining the efforts of astronomers, particle physicists and cosmologists, has been studied extensively throughout the years. In the prevailing description of cosmology, the Universe consists of three main components: ordinary matter, cold dark matter (CDM) and dark energy, the energy of vacuum space itself, associated with the cosmological constant Λ. Together these constituents are described and parameterized by the ΛCDM-model. In conjunction with ordinary matter, the cold dark matter is believed to have have condensed into small halos at an early epoch in the cosmic timeline (White and Rees, 1978; Jenkins et al., 2001; Guo et al., 2010). Over time, these objects must have undergone some form of hierarchical clustering, creating increasingly more massive systems. This 'bottom-up' approach to the formation of (proto-)galaxies predicts the abundance of small galaxies to be significantly higher than large galaxies, which is in qualitative agreement with observations. The large scale distribution of galaxies fits the general predictions provided by this formation scenario. Cosmological hydrodynamical simulations (Klypin et al., 2011; Pillepich et al., 2018) based on dark matter hierarchical clustering models are often used to study galaxy formation and evolution scenarios: there is a general good agreement between observations and simulations, but there are a few unsolved problems, explained in the last paragraph of this section.

One important property in galaxy evolution is angular momentum. Theory predicts that it was acquired by gravitational interactions with the environment. Studies explain that angular momentum was transferred to 'proto-galaxies' via their interaction with the tidal field of matter as it was aggregating into other proto-galaxies around them (Peebles, 1969; Bullock et al., 2001). The formation of galaxies at the center of dark matter halos is a result of gas cooling and fragmentation within the potential wells produced by the dark matter, such that gas condenses into the central parts of the halo where star formation is initiated. Eggen et al. (1962) first argued that by conservation of angular momentum, the gas' rotation increases radially inward during the cooling process. The contraction of gas in the radial direction is stopped by rotation, while the contraction in the z-direction continues, giving rise to a thin disk (Fall and Efstathiou, 1980; Mo et al., 1998). Elliptical galaxies, instead, are believed to be the result of mergers. For star-forming galaxies, both processes (i.e. star formation and angular momentum growth) continue throughout cosmic time, in such a way that stars formed at later times are also expected to be richer in angular momentum. This is a relevant notion in galaxy formation theories, which will be further enlightened in Sec. 1.2.

In this galaxy formation scenario, the assembly of stellar mass is predicted to advance from the central parts to the outskirts. Although the general description of the formation of dark matter halos is relatively well-established, the resulting theory explaining the growth of the luminous

components of galaxies has encountered a few problems. For example, cosmological hydrodynamical simulations have struggled for decades to produce a realistic population of disk galaxies having the correct angular momentum properties (Navarro and Steinmetz, 1997). Although modern models with increased resolution and highly efficient stellar feedback have reduced this problem (e.g. Marinacci et al., 2012; Lagos, 2018), the question remains debated (Pezzulli et al., 2017, and references therein). Another problem arises from the discrepancy between observed numbers of dwarf or satellite galaxies and the expected number from simulations, known as the 'missing satellite problem'. Perhaps one of the greatest problems in this field stems from the mismatch between low-mass galaxy density profiles derived from observations and predictions from ΛCDM simulations, formulated as the 'cusp-core problem'. Finally, another observed trend that is apparently inconsistent with the bottom-up approach is that low-mass galaxies experience their peak of star formation at a later epoch than higher mass galaxies, which is often referred to as 'downsizing' (Cowie et al., 1996). Bullock and Boylan-Kolchin (2017) provides a summary of these problems and possible solutions. More observational input is required for modelers to constrain galaxy formation and evolution scenarios. An important observational test comes from studying the growth of galaxy disks, which is the topic of this thesis. The way in which the stellar mass develops in a disk has strong connections with the galactic angular momentum and severe implications on galaxy formation and evolution models. In the following sections, different methods for analyzing disk growth and the adopted method in this work are described.

1.2 Size evolution of galaxies

The mean specific angular momentum of galaxies is thought to be an increasing function of time (Dutton and van den Bosch, 2012). The main conclusion to be drawn from this is that the outer parts of a galaxy (with higher specific angular momentum) should form later than the inner parts. In models of disk evolution, the inner parts of a disk are formed first. Then, as gas with larger angular momentum settles into the equatorial plane at increasingly large radii, stars are formed progressively outwards. Galaxy formation models (Ricciardelli and Franceschini, 2010; Aumer and White, 2013; Somerville and Davé, 2015; Pillepich et al., 2018) also predict the growth to advance from the inner to the outer parts: the 'inside-out' growth model. Several methods have been employed to test this theory, such as inspecting gradients (age, metallicity, color) in the disk, but there are multiple ways to quantify the phenomenon of inside-out growth. This section outlines some of the past efforts that have been made to quantify the radial growth of galaxies by either inspecting properties of the stellar distribution in individual disks (Sec. 1.2.1), or by evaluating the evolution of disk properties with redshift (Sec. 1.2.2).

1.2.1 Inside-out growth of star-forming galaxies

One obvious and relatively simple indicator of inside-out growth can be found in the color gradients of disks. Young stellar populations are, in general, bluer than older stellar populations. If a galaxy is found to be bluer in the outskirts than in the inner parts (a *negative* color gradient), then this observation suggests that more stars are being formed (relatively speaking) at larger radii than at small radii, which is in agreement with inside-out formation. Multiple studies have concluded that color gradients of their sample are consistent with inside-out growth. However, there are large variations in the gradients found by different authors. The main problem with this technique of using only colors lies in the difficulty of disentangling the effects of age, metallicity and dust extinction. For example, in a study of 142 nearby galaxies by Taylor et al. (2005), late-type galaxies overall showed to become redder towards the outskirts, with a larger total spread in color gradients. Despite this positive color gradient, Taylor et al. (2005) argue that these results can still be consistent with the hierarchical model, as mergers are predicted to be important and

occur frequently in this scenario. During merges, gas in the interacting galaxies can be funneled towards the center, triggering central star formation. More recently, Kennedy et al. (2016) analyzed galaxies from the GAMA survey and found that the vast majority exhibit bluer outskirts. Their sample is split into subcategories based on Sérsic index n (Sec. 1.3.1) and overall color. Fig. 1.1 shows the gradient ∇_{g-x} (where x is one of the bands r, i, z, Y, J, H) versus r-band absolute magnitude M_r. Noteworthy is that gradients generally become stronger for brighter galaxies and the only category of galaxies that show positive gradients is the blue, faint and high-n (more centrally concentrated) population.

It is clear that observational studies of disk growth are complicated by a large amount of factors. Other more recent studies confirm the inside-out growth model by finding negative (luminosity-weighted) age gradients (*i.e.* decreasing age of the stellar population with radius) in the majority of galaxies (Sánchez-Blázquez et al., 2014; González Delgado et al., 2015). This behavior is expected if star formation is to proceed in an inside-out manner, since new stars should form at progressively larger radii from the center. González Delgado et al. (2015) analyzed a sample of 300 galaxies in the nearby Universe drawn from the CALIFA survey. They computed mass- and light-weighted (luminosity-weighted) age gradients for this sample by fitting the spectral energy distribution (SED) with simple stellar population models. In Fig. 1.2, the light-weighted age gradients that they found are displayed. From both panels it is clear that most of the analyzed galaxies have negative age gradients. Furthermore, all averaged outer gradients are negative. Sd and Sc (late-type) spirals show more flattened gradients. The same holds true for the mass-weighted gradients. Additionally, (mass- and light-weighted) gradients for all types are stronger in the inner regions than in the outer regions, showing flattening after $\sim$ 1.5 half-light radius. This may be a signal of a more uniform growth in the outer regions of disks.

Very nearby galaxies, in which individual stars can be resolved, lend themselves well for studies of the color-magnitude diagram, used to derive star formation histories. Gogarten et al. (2010) analyzed the galaxy NGC 300 and found evidence for inside-growth. The stars in the inner parts of the disk are relatively old, and they concluded that the scale length (Sec. 1.3.1) increased by

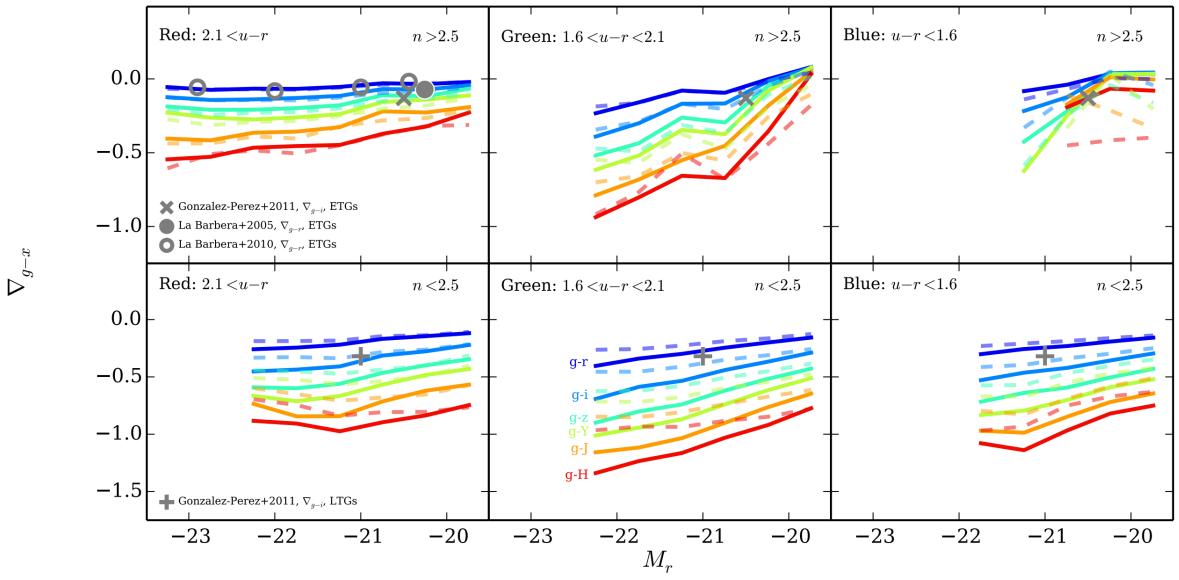

Figure 1.1: Figure from Kennedy et al. (2016) plotting color gradient ∇_{g-x} (where x is one of the bands r, i, z, Y, J, H, each indicated with a different color as shown in the bottom-middle panel) versus r-band magnitude M_r of red (*left*), green (*mid*) and blue (*right*) galaxies. Top panels represent galaxy populations with high Sérsic index n; bottom panels represent populations with low n. Solid and dashed lines are gradients over the ranges $0.1r_e - 1r_e$ and $0.1r_e - 2r_e$, respectively.

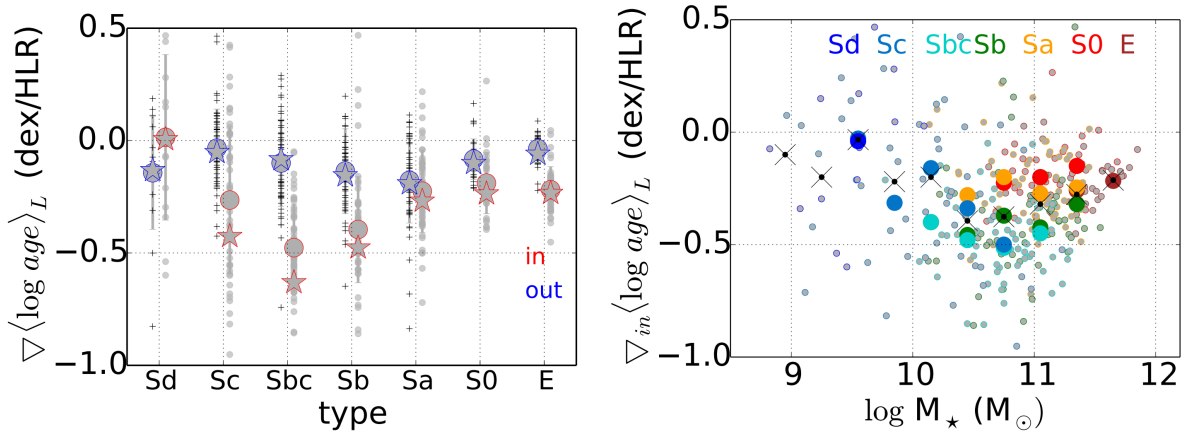

Figure 1.2: Figures from González Delgado et al. (2015) showing age gradients of the CALIFA galaxy sample. *Left panel*: Luminosity-weighted age gradients per morphological type. The distinction is made between the inner gradient (red-grey) and outer gradient (blue-grey), with the inner gradient being defined within the half-light radius (HLR), and the outer gradient between 1 and 2 HLR. Two stellar population models are used: *GMe* (stars) and *CBe* (circles). Large symbols represent the mean. *Right panel*: Inner luminosity-weighted age gradient as a function of stellar mass. Galaxies are color-coded based on morphological type (text in plot). Black crosses represent the relation between inner gradient and mass (independent on morphology). Large circles are the averaged inner gradients in stellar mass bins of 0.3 dex.

0.2 kpc in the last 10 Gyr. Other evidence for inside-out growth comes from spectral diagnostics (Li et al., 2015), metallicity gradients (Goddard et al., 2017), chemical evolution models (Mollá and Díaz, 2005), and derivations from the mass-size relation, for which more details are given in Sec. 1.2.2.

These observations demonstrate the complexity of the development of star formation in galaxies. From many studies it is clear that the assembly of stellar mass is affected by different processes. Hydrodynamical simulations (e.g. Aumer et al., 2014) have shown that processes such as gas infall and outflows, stellar migration, radial gas flows, and processes that govern star formation efficiency all influence the distributions of stellar populations in disks.

Another challenge that research in this field faces is the dependence of galaxy properties on redshift. Studies have shown that high-redshift galaxies are different from their local counterparts (e.g. Cooper et al., 2006; Behroozi and Silk, 2015), as galaxies are continuously evolving. The following section explains how this fact can also be exploited to gain information on galaxy disk growth.

1.2.2 Evolution of the mass-size relation

An important source of information that aids the understanding of galaxy growth comes from the mass-size relation. Galaxies appear to universally follow several empirical relations. One of the most well-established scaling relations is the Tully-Fisher relation (Tully and Fisher, 1977). This is a close correlation between the total luminosity and rotational velocity of spiral galaxies. Other scaling relations include the Fall relation (Fall, 1983) between specific angular momentum and mass, and the mass-size relation. The mass-size relation expresses to what degree the size of a galaxy correlates to stellar mass M_* and is usually described as a power-law:

$$R_* = AM_*^{\alpha}, \tag{1.1}$$

where A is a normalization factor, α is the power index, and R_* is a measure of galaxy size (e.g. effective radius or scale length; more details in Sec. 1.3.1). Since galaxies obey this general rela-

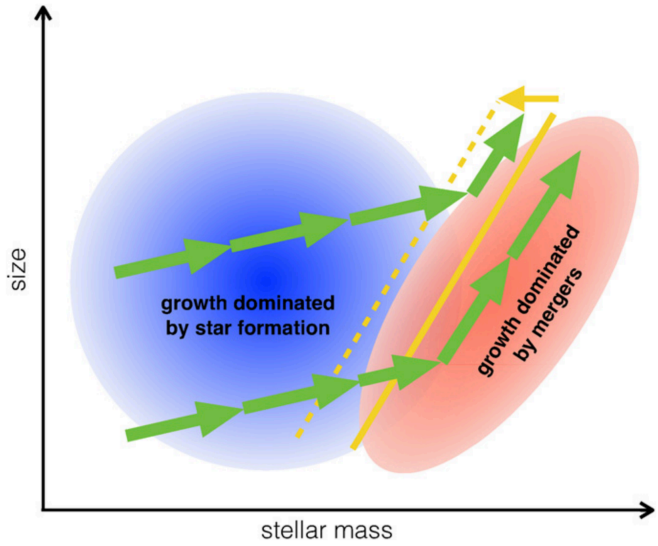

Figure 1.3: Illustration by van Dokkum et al. (2015) of average mass-size relation for star-forming (blue) galaxies evolving into quiescent (red) galaxies from $z \sim 3$ to $z \sim 0$. Star-forming galaxies move along the relation, growing mainly by creating new stars, until they reach a stellar density or velocity dispersion threshold (yellow line) which is redshift-dependent. This quenches star formation, after which the main growth process is determined by dry merging, taking the galaxies on a steeper track.

tion and stellar mass in star-forming galaxies only increases (as a consequence of star formation), this implies that, as galaxies increase in mass through star formation and merging processes, they also increase their size by moving along the relation. However, it is not fully understood if the relation is the same at every redshift. Research on the mass-size relation at different redshifts has lead to vastly different claims about its evolution, with some studies reporting little to no evolution (Ichikawa et al., 2012; Mosleh et al., 2020) while others claiming a moderate to strong evolution with z (van Dokkum et al., 2010; van der Wel et al., 2014; Nedkova et al., 2021). Despite this unresolved issue, there is mounting evidence that the slope of the relation is dependent on galaxy type, such that quiescent (early-type) and star-forming (late-type) galaxies follow distinctive tracks (van Dokkum et al., 2015; Dimauro et al., 2019). Several 'toy models' have been proposed to explain this behavior. In van Dokkum et al. (2015) a picture is described in which galaxies evolve on the track $R_* \propto M_*^{0.3}$ primarily by forming stars, up to the point at which they reach a critical stellar density or velocity dispersion that leads to quenched star formation. At this point, the galaxies become quiescent, where their growth is mainly compelled by dry mergers, leading to a steeper mass-size track. Dry mergers are mergers where star formation is not enhanced after the event. Fig. 1.3 illustrates how these galaxies move in the size-mass plane.

Coming back to the evolution of the mass-size relation, quantifying how the normalization A varies with redshift provides a description of the rate at which galaxies grow in size. This can be specifically expressed in terms of how the median size in a fixed mass bin changes with redshift. Mowla et al. (2019), for example, find that massive ($M_* > 2 \times 10^{11}\,\mathrm{M}_\odot$) star-forming galaxies have significantly increased their size since $z \sim 3$, and parameterize this as $r_e/\mathrm{kpc} = 25.4 \times (1+z)^{-1.40}$. In this equation, r_e is the effective radius.

Two important conclusions can be drawn from the mass-size relation under the assumption that star-forming galaxies grow inside-out. There are two possible scenarios: the mass-size relation is universal, or it evolves with redshift (increasing normalization with cosmic time). Considering the first scenario, from this directly follows that galaxies should grow inside-out at the rate necessary to remain on the mass-size relation. If, on the other hand, the mass-size relation is also evolving

with redshift, then this implies that the inside-out growth of galaxies is even faster.

1.3 SFRD fitting method

In this research, a method proposed by Pezzulli et al. (2015) (P15, hereafter) is adopted that looks for an instantaneous signal of disk growth. It exploits the shape of the distribution of stellar mass in disks, which has been shown to be well-characterized by an exponential profile since early times; from at least $z \sim 6$ (Fathi et al., 2012). Since star formation is an ongoing process in disk galaxies, the distribution of new-born stars in a disk can be used as a direct proxy for its growth process. The method consists of two parts: the distribution of stars in the disk is modeled to infer the disk size, after which the distribution of star formation is modeled to infer the rate at which the disk grows. In the next sections, tracers of the stellar distribution and star formation are highlighted, after which the method is described in its entirety.

1.3.1 Tracing stellar distribution

Light has to satisfy a few conditions in order to serve as a probe for the stellar distribution in a galaxy: it has to be emitted predominantly by long-lived stars and it must not considerably suffer from attenuation. Near infrared (NIR) light is often considered a good probe, since most of a galaxy's NIR radiation is emitted by long-lived stars and there is not much contamination from other sources. Furthermore, NIR light does not suffer much absorption from dust. In fact, the interstellar extinction curve (which describes the dependence of dust attenuation on wavelength) roughly increases with λ^{-1}, meaning that dust absorption becomes increasingly stronger at shorter wavelengths and reaches its peak in the optical – ultraviolet (UV) (Piovan et al., 2006). Defining the size of a disk from its stellar distribution is not a straightforward process. The difficulty lies in the fact that the boundary of a disk is hard to define. The distribution of stars (and thus light) inside the disk roughly follows an exponential profile – there is no hard 'edge' of a disk. Therefore, different measures for disk size have been proposed. Two of the most commonly used measures are the half-light radius and exponential scale length. The half-light or effective radius r_e is the radius at which half of the total light of the galaxy is emitted. It also appears in some mathematical functions describing the brightness profile of galaxies, such as the Sérsic profile (Sérsic, 1963) and the de Vaucouleur profile (de Vaucouleurs, 1948). The Sérsic profile describes the intensity I at radius R, such that:

$$I(R) = I_e \exp\left\{-b_n\left[\left(\frac{R}{r_e}\right)^{1/n} - 1\right]\right\}, \tag{1.2}$$

where I_e is the intensity at r_e, n is the Sérsic index controlling the shape of the profile, and b_n is approximately equal to $2n - \frac{1}{3}$ (Ciotti, 1991). The de Vaucouleur profile is a special case of the Sérsic profile, for $n = 4$. An exponential profile is also a special case of the Sérsic profile for $n = 1$. In this case, there exists a relation between the half-light radius and scale length R_s:

$$r_e = 1.678\, R_s. \tag{1.3}$$

The scale length is the radius at which a galaxy's brightness is a factor e (≈ 2.72) lower than the central brightness.

1.3.2 Tracing star formation

Among possible tracers of star formation in galaxies, one that has been extensively used is the hydrogen Hα emission line. The main mechanism for the production of Hα is the following. The

ultra-violet radiation from massive stars ionizes the surrounding gas. Then, as the free electrons are re-captured by the ions and cascade down in energy, radiation is emitted through recombination lines, among which, Hα. In the integrated galaxy spectra, star-forming galaxies show prominent spikes at the positions of these lines. Only relatively massive and young stars ($M \gtrsim 10_{\odot}$ and age $\lesssim 20\,$Myr) contribute to the ionizing flux. The strength of these lines therefore grants a direct probe of the young massive stellar population (Kennicutt, 1998). Hα, in particular, has several advantages over other emission lines: it is easily detectable in most galaxies, it does not suffer as much absorption from dust as other lines (although also for Hα extinction is not insignificant), and its emission is predominantly associated with star-forming regions. With an evolutionary spectral synthesis model of stellar populations, an observed Hα luminosity ($L_{\mathrm{H}\alpha}$) can be converted to a star formation rate (SFR or $\dot{M}_*$) where the connection is given through the rate of production of ionizing photons. The result is dependent on the choice for the initial mass function (IMF). This function describes the distribution of masses in stellar populations at birth. In this work we adopt the conversion from Hα luminosity to SFR from Kennicutt and Evans (2012), which assumes an IMF presented in Kroupa and Weidner (2003). Their calibrations yield:

$$\log\left(\dot{M}_*\,[\mathrm{M}_{\odot}\,\mathrm{yr}^{-1}]\right) = \log\left(L_{\mathrm{H}\alpha}[\mathrm{erg\,s}^{-1}]\right) - \log(41.27). \tag{1.4}$$

Other commonly used tracers of star formation include forbidden lines (such as [OII]), and far ultraviolet (FUV) wavelengths where the spectrum is dominated by radiation from young stellar populations. When probing local galaxies, UV wavelengths are inaccessible for ground-based telescopes, but when probing galaxies at $z \gtrsim 1$ these wavelengths shift to the optical/NIR such that they can be observed from the ground. SFR indicators making use of the optical or UV emission of galaxies need to be corrected for dust. Emission at these wavelengths is partially absorbed by dust, which then re-emits the absorbed emission in the IR. Some SFR indicators (e.g. $24\,\mu$m or total IR) have been proposed that make direct use of IR emission, treating it as a calorimeter that measures the total power produced by young stellar populations (Rieke et al., 2009). Other works combine indicators in the UV, optical and IR to improve the accuracy of SFR measurements (e.g. Calzetti et al., 2007).

Measuring the SFR in spatially resolved regions of a galaxy allows us to obtain the star formation rate surface density (SFRD). The determination of the SFRD as a function of radius gives us a SFRD profile which often displays a nearly exponential shape. This hints at a connection between star formation and the underlying mechanism responsible for the exponential disk structure. The first endeavor in this direction was made by Muñoz-Mateos et al. (2007), who derived specific (normalized by stellar mass) star formation rate (sSFR) profiles from ($FUV - K$) color profiles of 161 nearby galaxies, similar to color-gradient methods highlighted in Sec. 1.2.1. The gradient of these profiles was used to quantify the inside-out formation: sSFR should increase with increasing radius if star formation progresses inside-out. The underlying assumption in this work is that both the stellar mass surface density (SMSD) and SFRD can be approximated by distinct exponential profiles, characterized by different scale lengths. Often, however, the SFRD profile is not exactly exponential. In many cases, local galaxies show an inner depletion of star formation relative to the exponential shape, explained by the fact that most of the star formation in the central regions of the disk happens early on (in line with the inside-out formation scenario). In the next section, a description of the P15 model is provided.

1.3.3 Model

Following the assumptions presented in P15, we say that the stellar mass surface density of galaxy disks at every time is well-described by an exponential profile Σ_*, characterized by the total stellar

mass M_* and scale length R_s:

$$\Sigma_*(t,R) = \frac{M_*(t)}{2\pi R_s(t)} \exp\left[-\frac{R}{R_s(t)}\right], \tag{1.5}$$

where both M_* and R_s are functions of time. A prediction for the star formation rate surface density is obtained by taking the time derivative of this function:

$$\dot{\Sigma}_*(t,R) = \left[\nu_M + \nu_R\left(\frac{R}{R_s(t)} - 2\right)\right]\Sigma_*(t,R). \tag{1.6}$$

This yields a combination of a linear and exponential function where ν_M and ν_R are defined as:

$$\nu_M = \frac{\mathrm{d}}{\mathrm{d}t}(\ln M_*(t)) = \frac{\dot{M}_*}{M_*}, \tag{1.7}$$

$$\nu_R = \frac{\mathrm{d}}{\mathrm{d}t}(\ln R_s(t)) = \frac{\dot{R}_s}{R_s}. \tag{1.8}$$

By following this approach, two measures for galaxy growth are retrieved: the specific mass growth rate ν_M and radial growth rate ν_R. The word 'specific' refers to the fact that these quantities are normalized by mass and size, respectively, which allows for a direct comparison between galaxies. From this point onward, equations 1.5 and 1.6 will be referred to as *SMSD model* and *SFRD model*, respectively. The two 'ingredients' for retrieving the growth rates via the SFRD model thus are the scale length and a profile or map of the SFRD. The scale length may be inferred from fitting the SMSD model on a profile or map of the stellar surface density. The values for the mass and radial growth rates can subsequently be obtained via fitting the SFRD model. This is the basis of the research in P15 and in this work, with two differences being that P15 worked at $z = 0$ while we are performing the same experiment at $z = 1$, and that P15 use FUV emission to trace star formation, while we use Hα. The assumed cosmology throughout the analysis is flat ΛCDM, with values for the parameterization: $H_0 = 70\,\mathrm{km\,s^{-1}\,Mpc^{-1}}$, $\Omega_M = 0.27$, $\Omega_\Lambda = 0.73$.

There are two main assumptions underlying this approach. Taking the time derivative of Σ_* gives a *rough* prediction for the SFRD. The continuity equation states that the generation of a quantity q (M_* in this case) per unit volume and time (σ) is equal to the sum of the time derivative of the density (ρ) of q and the divergence of the flux of q. In an equation this becomes:

$$\frac{\partial \rho}{\partial t} + \boldsymbol{\nabla} \cdot \vec{j} = \sigma, \tag{1.9}$$

where $\vec{j}$ is the flux of q. In our treatment we have $\dot{\Sigma}_* = \frac{\partial \Sigma_*}{\partial t}$, corresponding to the first term on the left hand side of Eq. 1.9, while net radial migration of stars (represented by the term $\boldsymbol{\nabla} \cdot \vec{j}$) is not taken into account. However, it has been shown that the main mechanism behind radial migration is the exchange of the positions of two stars, resulting in no net migration (Sellwood and Binney, 2002; Roškar et al., 2012).

The rate of change of the stellar mass distribution is in general different from the SFRD also for another reason. In the course of its lifetime, a star transfers a non-negligible amount of mass back to the interstellar medium (ISM). To correct for this, $\dot{\Sigma}_*$ represents the *reduced* star formation rate surface density: SFRD $\times (1 - \mathscr{R})$. Here, $\mathscr{R}$ represents the return fraction of mass from stars to the ISM, where we have used the instantaneous recycling approximation (Cimatti et al., 2019). In this analysis we assume a constant return fraction of $\mathscr{R} = 0.3$, an intermediate value between choices of the initial mass function (IMF) (Fraternali and Tomassetti, 2012). When in the remainder of this thesis the quantity SFRD is mentioned, it should be interpreted as *reduced* SFRD.

A short note about Eq. 1.7 is that the specific mass growth rate, or ν_M, is related to another quantity: the specific star formation rate, which has been extensively investigated for galaxies in

the nearby and high-redshift Universe (Salim et al., 2007; Wuyts et al., 2011; Curtis-Lake et al., 2013). Two differences should however be kept in mind, the first one being that ν_M only refers to the disk; not the whole galaxy. Furthermore, since ν_M and ν_R are derived from the reduced SFRD (including a return fraction $\mathscr{R}$), the quantity ν_M corresponds to the *reduced specific* SFR of the disk.

Predicted profiles

In Fig. 1.4, the 1D (radial) profiles for three values of the radial growth rate are showcased to illustrate the resulting shapes of the SFRD as a function of radius. The solid red line represents a disk which is growing in size. Moving from the outer to the inner parts, the SFRD is roughly exponential to a radius of $\sim 2R_s$ ($R_s = R_*$ in this figure), but its slope declines inward of this point: an inner depletion. Star formation is proceeding at a relatively slower (specific) rate in the central parts compared to the outskirts. The black dotted line is a case where there is no radial growth of the disk. Looking at Eq. 1.6, the second term inside the square brackets vanishes, leaving only the product of the mass growth rate and the SMSD: an exponential profile. Finally, the behavior of a shrinking disk is depicted by the blue dashed line, where the shape of the SFRD is roughly exponential in the inner regions, but it drops off after $\sim 2R_s$, as the second term inside the square brackets in Eq. 1.6 takes over. This means that the specific star formation rate is low at large radii compared to small radii, which implies that the assembly of new stellar mass happens faster in the inner regions compared to the outer regions.

1.3.4 Previous results

P15 analyzed a sample of 35 nearby star-forming galaxies by fitting the model on radial profiles of SMSD and SFRD obtained using high-quality NIR to FUV data from the Spitzer/IRAC 3.6 μm band and GALEX FUV band respectively, including a dust correction based on FIR (profiles published by Muñoz-Mateos et al., 2009b,a). They retrieve a positive radial growth rate in 32 cases. Most

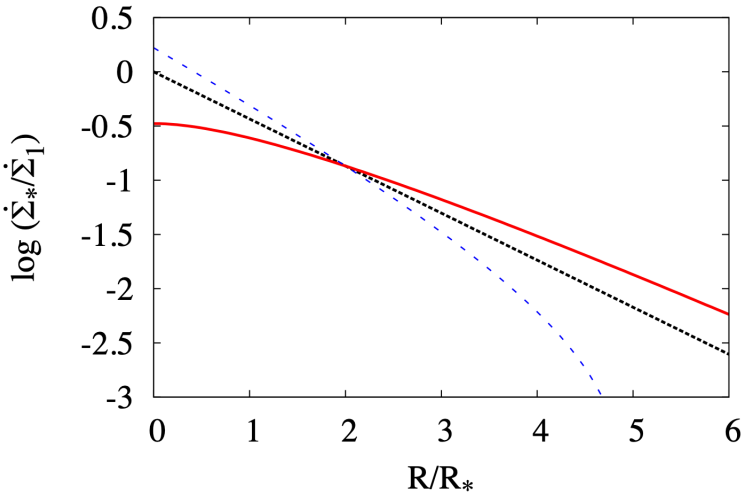

Figure 1.4: Figure from Pezzulli et al. (2015) displaying the predicted shapes of the SFRD in dimensionless units for three cases for the radial growth rate: growing disk with $\nu_R = \frac{1}{3}\nu_M$ (solid red line), no growth of the disk with $\nu_R = 0$ (black dotted line) and shrinking disk with $\nu_R = -\frac{1}{3}\nu_M$ (blue dashed line). Note that the radius is normalized to the scale length R_* and $\dot{\Sigma}_*$ is normalized to $\dot{\Sigma}_1 = \nu_M M_*/(2\pi R_*^2)$, such that the comparison of the trends refers to disks with the same stellar mass, scale length and global sSFR.

galaxies have a mass growth rate of $\sim 0.1\,\mathrm{Gyr}^{-1}$ which corresponds to a mass growth timescale of $\sim 10\,\mathrm{Gyr}$. This is in agreement with other studies investigating the main sequence of star formation (SFR versus stellar mass, Elbaz et al., 2011). Galaxies were found, by P15, to grow in size on average at about $\frac{1}{3}$ of the rate at which they grow in mass, corresponding to a radial growth timescale of $\sim 30\,\mathrm{Gyr}$. There are six galaxies in this sample with a comparatively low mass growth rate ($\log \nu_M < -1.6\,\mathrm{Gyr}^{-1}$), but they are all relatively early-type spirals. P15 explain that this may be a sign of downsizing (Sec. 1.1, Cowie et al. (1996)): high-mass early-type galaxies ran out of gas to form new stars at earlier epochs which means there is little residual star formation. From the fact that 32/35 galaxies have $\nu_R > 0$, P15 conclude that their results are consistent with inside-out growth still occurring at $z \simeq 0$. Implications from their plot of ν_R versus ν_M are related to the evolution of the size-mass relation. Eq. 1.1 describes how size and mass are related through a power-law: $R_s = AM_*^{\alpha}$. If both the normalization A and coefficient α are not evolving with time, the size-mass relation is universal. P15 found that ν_R and ν_M agree with a relation $\nu_R = \alpha\,\nu_M$, as expected for galaxies growing along the mass-size relation (Eq. 1.1), which in turn they interpreted as an indication that the relation itself is not evolving in time.

1.3.5 Aim of this work

The aim of this work is to extend the methodology described above (so far only applied at $z \simeq 0$, which substantiates the necessity to extend research on this topic beyond local galaxies) and measure the specific radial growth rate of star-forming galaxies at $z \simeq 1$. Instead of using UV emission to trace star formation, we use Hα, which is less affected by dust compared to UV emission. Fortunately, IFU spectroscopy (explained in more detail in Chapter 2) has allowed for spatially resolved studies of the SFRD at increasingly higher redshifts. Two major IFU surveys of galaxies at $z \simeq 1$ are KMOS^{3D} (Wisnioski et al., 2019) and KROSS (Stott et al., 2016), both making using of the K-band Multi-Object Spectograph (KMOS). In this thesis, we aim to quantify the mass and radial growth rates of individual star-forming galaxies at $z \simeq 1$ by applying the SFRD fitting method from P15 to a sample of galaxies from the KROSS survey, studied earlier by Di Teodoro et al. (2016) and by Marasco et al. (2019), who provide stellar disk scale lengths from HST observations. The data products provided by KROSS are comprised of spatially resolved spectra (data cubes) in the YJ band, which includes the Hα line at $z \simeq 0.8 - 1$. We use these products to construct maps of Hα to examine the distribution of the star formation rate in our sample. Instead of fitting radial profiles extracted from intensity maps, we fit the maps directly in 2D. This enables us to better account for the observational effects, in particular the spatial resolution of our data.

1.3.6 Caveat about dust absorption

UV and optical measurements are complicated by interstellar dust absorption, which causes a portion of the light to be re-emitted in the IR. Hence, intrinsic UV/optical lines are in general brighter than measured values. A spatially uniform extinction would not affect the reliability of our method. However, analyses of dust extinction in galaxies show that the rate at which the surface density of dust declines with radius r is similar to the rate at which the SMSD declines with r, but slower than the rate at which the SFRD declines with r (Smith et al., 2016). As such, it is likely that dust is not uniformly distributed and this could introduce a bias. A reliable technique for estimating interstellar extinction is the measurement of the Balmer decrement: Hα/Hβ (e.g. Domínguez et al., 2013). The value of the Balmer decrement is set by quantum physics, such that a deviation from this value may be attributed to dust. However, the technique cannot be applied in this work as the wavelength of the Hβ line is not included in the YJ band at $z \simeq 1$.

1.4 Outline of the thesis

In Chapter 2, one can read a description of the extraction of Hα maps. The 2D fitting procedure is applied on a test sample, including a comparison with results of previous work on the same sample. In Chapter 3, the adopted galaxy sample is described, alongside further data reduction and calibrations. In Chapter 4 the results are presented, along with a discussion of their implications, uncertainties and possible improvements. Finally, in Chapter 5, a summary of our analysis is provided, our final conclusions are stated and future prospects are discussed.

Chapter 2

2D fitting of Hα maps

Before committing to the inference of galaxy growth rates using the model outlined in Sec. 1.3.3, we first describe our fitting routine and establish that it works well and produces robust results. This is done by fitting a simple 2D exponential profile to a small set of Hα maps. Because the procedure is profoundly similar to the one presented in Wilman et al. (2020) (W20, hereafter), the routine is tested by comparing with their results, where galaxies of the KMOS^{3D} survey (Wisnioski et al., 2019) are analyzed. W20 take a subset of 281 galaxies from the original sample and derive half-light sizes by fitting 2D exponential profiles, convolved with the observational point spread function, to Hα maps. In this chapter, the methods for extracting Hα maps from KMOS data are explained, and the construction and fitting of an axisymmetric exponential model on these maps are described. Lastly, a check of the fitting strategy is presented by comparing results for a small sample of galaxies analyzed in W20.

2.1 Data

2.1.1 KMOS instrument and data

The *K*-band Multi-Object Spectrograph, or KMOS, is an instrument that operates on the ESO Very Large Telescope (VLT) at the Paranal Observatory in Chile. Its main feature is its ability to obtain spatially resolved spectra for 24 targets simultaneously in the NIR bands, by performing integral field spectroscopy, i.e. combining imaging with spectrographic capabilities. The instrument utilizes 24 separate arms, each equipped with an integral field unit (IFU). A picture of this setup is shown in Fig. 2.1a. Light from user-specified sub-fields is fed to the individual IFUs, which slices it into 14×14 spatial pixels. Spectra are then obtained for each pixel, via the dispersion of the signal by a cryogenic grating spectrometer. KMOS is equipped with three of these spectrometers, each having a slightly different wavelength coverage due to the spectral curvature, which is corrected for as part of the data reduction pipeline. The IFUs on KMOS have a field of view (FOV) of $2.8'' \times 2.8''$, meaning that a single pixel covers an area of $0.2'' \times 0.2''$. An exposure with KMOS generates spectra in each of these *spatial* pixels with 2048 pixels along the spectral axis. That is, a spectral pixel represents the smallest resolvable element $\Delta\lambda$, which is dependent on the employed band (Tab. 2.1). Data from KMOS hence contain information on a three-dimensional grid of size $14 \times 14 \times 2048$. These data are stored in a format called 'data cube', which in general is an N-dimensional array of values. In this format, the word 'channel' is used to describe a pixel in the spectral direction. Every spatial pixel essentially contains an entire spectrum obtained in a $0.2'' \times 0.2''$ FOV. In turn, one channel map shows the intensity of a target in an interval $\Delta\lambda$ around a certain wavelength in a FOV of $2.8'' \times 2.8''$. A data cube is represented as $C(x, y, z)$ in this work: two spatial axes x and y, and one spectral axis z. A schematic view of a data cube is shown in Fig. 2.1b.

band	wavelength coverage (μm)	pixel scale (nm/pixel)
HK	1.484 – 2.442	0.489
K	1.934 – 2.460	0.266
H	1.456 – 1.846	0.203
YJ	1.025 – 1.344	0.165
IZ	0.779 – 1.079	0.143

Table 2.1: Wavelength coverage and pixel scale of the five employable bands on the KMOS instrument. Information is taken from ESO (2013).

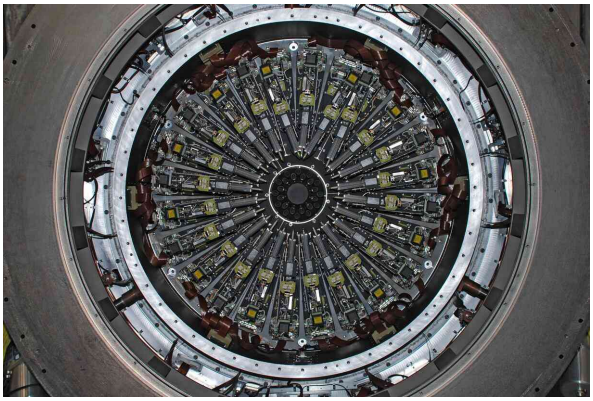

(a)

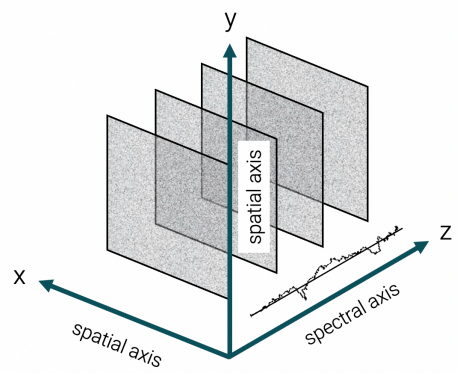

(b)

Figure 2.1: a) Picture of the 24 configurable arms in the front end of the KMOS cryostat, each equipped with an IFU. Image taken from ESO (2013). **b)** Visualization of data storage in a data cube, with the pixels (x- and y-direction) representing spatial coordinates on the sky of a certain angular width and different channels (z-direction) representing windows of a certain spectral width.

2.1.2 Hα map extraction

The Hα emission line, with a rest-frame wavelength sitting at $\lambda_{\mathrm{H}\alpha,\mathrm{rest}} = 0.656\,28\,\mu$m, is the main line present in our data cubes. Depending on the redshift of the galaxy, the observed wavelength shifts to a larger wavelength $\lambda_{\mathrm{H}\alpha,\mathrm{obs}}$, according to

$$\lambda_{\mathrm{obs}} = (1+z)\lambda_{\mathrm{rest}}. \tag{2.1}$$

The channel containing the observed wavelength $z_{\mathrm{H}\alpha}$ can simply be found by using the pixel scale $\Delta\lambda$ and the starting wavelength of the band λ_i:

$$z_{\mathrm{H}\alpha} = \frac{\lambda_{\mathrm{H}\alpha,\mathrm{obs}} - \lambda_i}{\Delta\lambda}. \tag{2.2}$$

Here, $z_{\mathrm{H}\alpha}$ indicates the spectral coordinate of the Hα line in the cube, not to be confused with the redshift. However, emission lines are broadened by several processes, including the rotational velocity of the galaxy itself, but also instrumental broadening effects such as beam smearing: broadening as a result of the low spatial resolution. Since the channel widths are of the order of tenths of nanometers (corresponding to $\sim 40\,\mathrm{km\,s^{-1}}$ in velocity), the Hα line most often occupies more than one channel. This is shown in Fig. 2.2a. To include all the emission, we visually

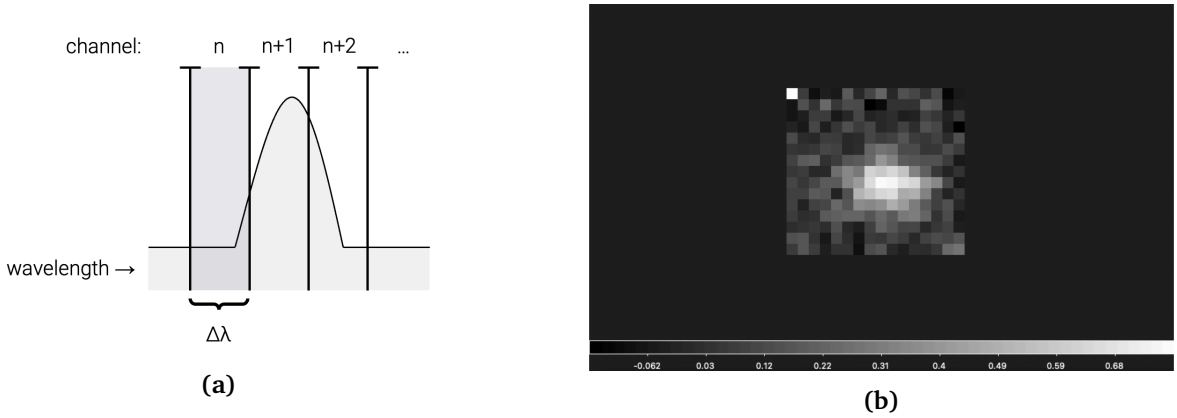

(a) **(b)**

Figure 2.2: a) Diagram showing how a spectral pixel (channel) represents a window of certain width $\Delta\lambda$ in the total spectrum obtained in one spatial pixel. **b)** Channel in the data cube of a galaxy from the KMOS^{3D} survey (GS4_12401) showing clear Hα emission. SAOImageDS9 (Joye and Mandel, 2003) is used to display the data cube. Units of the cube are W m^2 μm^{-1}.

inspect the data cube and cut it at two positions along the spectral axis: z_1 and z_2, the first and last channel in the cube with Hα emission. We remove all channels below z_1 and above z_2. The result is the cube $C_{\mathrm{H}\alpha}(x, y, [z_1 : z_2])$ that spans a wavelength range of λ_1 to λ_2, corresponding to z_1 and z_2. An example of a galaxy where Hα emission is clearly visible in its data cube is shown in Fig. 2.2b. The software BBAROLO (Di Teodoro and Fraternali, 2015) is then used to extract total flux maps from the cubes $C_{\mathrm{H}\alpha}(x, y, [z_1 : z_2])$ for each galaxy. BBAROLO outputs the maps with flux units in terms of the original flux units, multiplied by the channel width Δv in km s^{-1}. We denote the Hα map by $M_{\mathrm{H}\alpha}(x, y)$.

2.2 Model creation and fitting

2.2.1 Model definition

A 2D axisymmetric model is defined with a certain number of free parameters, fixed parameters depending on the galaxy and a set of independent variables, which is used as the coordinate input. Fixed parameters concern the geometry of the disk and the seeing conditions at the moment of observing (more details in next subsection). The geometrical parameters consist of the coordinates of the center in the image (x_c, y_c), the inclination i and position angle θ. Coordinates in the image (x, y) are transformed to coordinates in the plane of the disk (x', y'), using the fixed geometrical parameters belonging to each galaxy. The free parameters are left to vary such that a fitting routine can be used to find their best values. The following coordinate transformations are applied to go from coordinates in the plane of the image to coordinates in the plane of the disk:

$$x' = \cos\theta(x - x_c) + \sin\theta(y - y_c) \tag{2.3}$$

$$y' = \frac{1}{\cos i}[-\sin\theta(x - x_c) + \cos\theta(y - y_c)]. \tag{2.4}$$

In this system, the coordinates of the center are $(x'_c, y'_c) = (0, 0)$. All coordinates are rotated by the position angle θ. However, this effect only becomes apparent for an inclined disk. In an axisymmetric model, all quantities can be expressed as a function of R, which is the galactocentric radius:

$$R = \sqrt{(x')^2 + (y')^2}, \tag{2.5}$$

where R is converted from pixel units to kpc by using the transverse separation in proper kpc per arcsecond at redshift z. The AstroPy function `kpc_proper_per_arcmin` is used for this conversion. In this way, each set of coordinates in the image is mapped to a set of coordinates in the plane of the disk, corresponding to a certain radius R. The radius R is subsequently fed into the axisymmetric function $f(R)$, which outputs the amplitude of the function on a grid equal to the size of the image.

Point Spread Function

Included in the definition of the model is the convolution of the output of function $f(R)$ with a point spread function (PSF) to account for atmospheric seeing. A PSF can be seen as the function that describes how a point source is smeared out in an image. Earth observations suffer from a certain amount of blurring due to turbulence in the atmosphere. To simulate the same amount of blurring in the model, the output of the function $f(R)$ is convolved with the PSF. A PSF is best described by a probability density function. Lorentzian or Gaussian distributions are usually good candidates, but the Moffat distribution (Moffat, 1969) is sometimes preferred if the wings of the PSF are not accurately described by either of the aforementioned profiles. Seeing measurements often refer to the full width at half maximum (FWHM) of the 'atmosphere's PSF'. For the low resolution maps we are modeling, it suffices to assume that the PSF is Gaussian:

$$\mathrm{PSF}_{\mathrm{Gauss}}(x,y) = A \cdot \exp\left\{-\left[\frac{(x-x_0)^2}{2\sigma_x} + \frac{(y-y_0)^2}{2\sigma_y}\right]\right\}, \tag{2.6}$$

where A is the normalization, x_0 and y_0 are the central coordinates, and σ_x and σ_y are the standard deviations along x and y. The shape of the PSF is elliptical or circular, depending on the particular seeing conditions. In the latter case the function has equal width in x- and y-direction ($\sigma = \sigma_x = \sigma_y$). The standard deviation is related to the FWHM, as

$$\sigma = \frac{\mathrm{FWHM}}{2\sqrt{2\ln 2}}, \tag{2.7}$$

where the FWHM is, in our case, equal to the seeing at the moment of the observation, transformed from arcseconds to pixel units. The convolution of the two functions f and PSF is an integral transform that generates a third function $h = f * \mathrm{PSF}$, describing how f is modified by the PSF. In an equation, this is denoted as:

$$(f * \mathrm{PSF})(t) = \int_{-\infty}^{\infty} f(u)\,\mathrm{PSF}(t-u)\,\mathrm{d}u\,. \tag{2.8}$$

In essence, Eq. 2.8 expresses the area under $f(u)$ weighted by PSF$(-u)$ after a shift of t. The output of $f(R)$ is convolved with the Gaussian PSF as in Eq. 2.6, where the built-in AstroPy filter `Gaussian2DKernel` from the convolution module is used to define $\mathrm{PSF}_{\mathrm{Gauss}}$. Fig. 2.3 shows the difference between a model with and without including its convolution with a 2D Gaussian PSF. The FWHM is assumed to be fairly large here ($1'' = 5$ pixels) to demonstrate the difference between the two.

2.2.2 Minimization routine

Fitting weights

Before the Hα maps are fitted with the model, we determine which pixels of the map contain trustworthy emission. This is done by applying a threshold that selects the pixels that are reliable for the fitting procedure. For example, a mask may be created using a signal to noise (S/N)

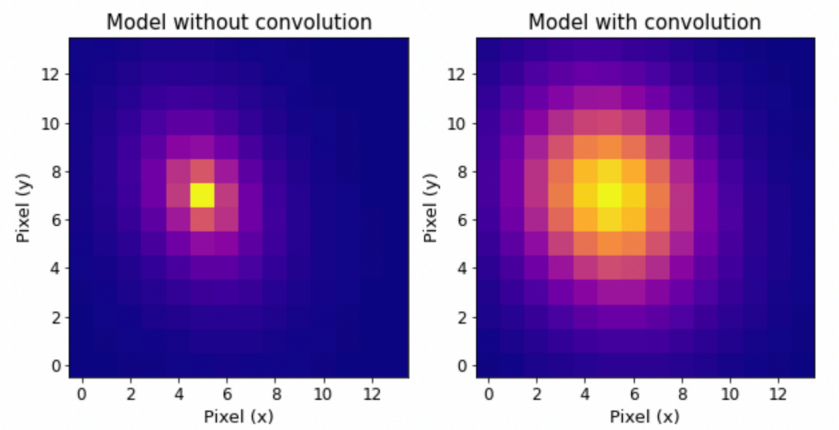

Figure 2.3: On the left is a model without convolution; on the right is the same model convolved with a 2D Gaussian PSF (FWHM $= 1''$, corresponding to 5 pixel units).

threshold. Here, the S/N of a pixel is calculated by dividing the value of the pixel in units of the map by the noise in the map in the same units. Pixels above the threshold receive a weight of 1; pixels below the threshold get a weight of 0 and hence, are not fitted. In this way we create a mask of weights that is applied during the fitting routine.

Chi-square

The 2D axisymmetric models are fitted to the Hα maps using the Levenberg-Marquardt (LM) algorithm from the curve-fitting code LMFIT (Newville et al., 2014). This is essentially a wrapper around the `curve_fit` module from SciPy, but allows for more direct control of the parameters, such as user-specified fitting boundaries for the free parameters. The LM algorithm is also known as the damped least-squares method and is used to solve non-linear least-squares problems. Problems of this category involve minimizing the sum of the squares of the residuals; finding the best-fit model to 2D image data can essentially be reduced to a least-squares problem. In general, the χ^2 statistic is defined as a measure of the quality of the fit on observations O with model M:

$$\chi^2 = \sum_i w_i (O_i - M_i)^2 , \tag{2.9}$$

where O_i and M_i are points in the sets of observational data and modeled data, respectively, and w_i is the weight of data point O_i. The weight is often defined as the inverse of the variance σ_i^2. However, this assumes that the uncertainty for each observational data point is known. In this work, weights are defined as explained in the previous subsection. The Levenberg-Marquardt solver is used to find values for the free parameters of the model such that χ^2 is minimized. Reported standard errors of 1σ for fitted parameters are those values that increase χ^2 by the *reduced* chi-square statistic:

$$\chi^2_\phi = \frac{\chi^2}{\phi}, \tag{2.10}$$

where ϕ is the degrees of freedom (*i.e.* the number of observations minus the number of free parameters). This means that, if the minimized chi-square is found ($\chi^2_{\rm min}$), the error σ_q on a fitted parameter q is determined by finding:

$$q \pm \sigma_q \quad \text{such that} \quad \chi^2(q \pm \sigma_q) = \chi^2_{\rm min} + \chi^2_{\phi,{\rm min}}. \tag{2.11}$$

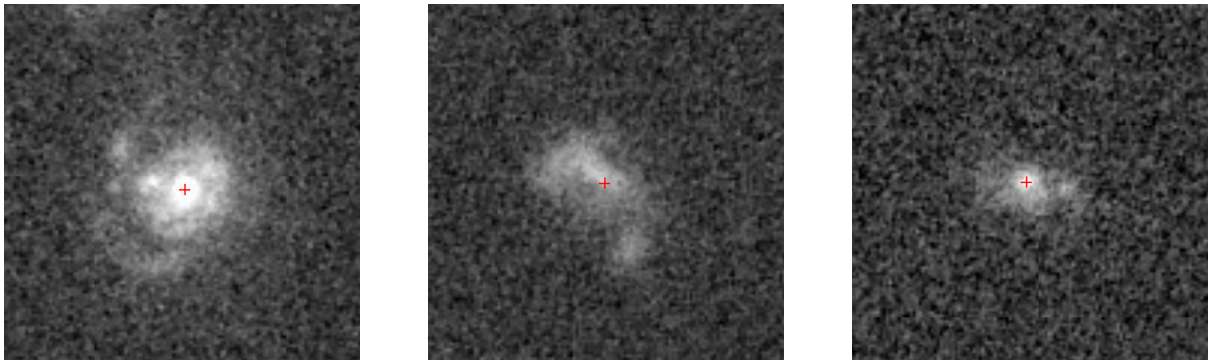

(a) GS4_12401 **(b)** U4_12959 **(c)** U4_19754

Figure 2.4: HST images (F814W filter) of the test galaxy sample, taken from the CANDELS survey (Grogin et al., 2011; Koekemoer et al., 2011). Galaxy names are the same as used in the KMOS^{3D} survey. The red crosses indicate the centers of the galaxies.

2.3 Test on a small sample

In this section we describe how we test the fitting routine. W20 derive half-light radii r_e for a sample of 281 galaxies from the KMOS^{3D} survey by fitting exponential functions to the Hα emission maps. We remind that the scale length R_s and r_e are linearly related (Eq. 1.3). Analogously to W20 we obtain the scale length for a galaxy by fitting an exponential function, convolved with the correct PSF, of the form:

$$f(R) = K \exp\left(-\frac{R}{R_s}\right), \tag{2.12}$$

where $f(R)$ is the flux at galactocentric radius R (Eq. 2.5) and K is the normalization. We compare our found scale lengths for a small sample of three galaxies with those found by W20 to asses if the fitting routine is robust. 1D radial profiles are extracted from the map and model in elliptical annuli, both in W20 and in this work, since the model does not produce azimuthal variations. These are used to judge the quality of the fits, as clarified in Sec. 2.3.3.

2.3.1 KMOS^{3D} survey

KMOS^{3D} is a near-IR spectroscopic survey of more than 700 galaxies, using the multi-IFU on KMOS (Davies et al., 2013; Sharples et al., 2013, and Sec. 2.1.1). The survey was conducted to study the physical mechanisms driving the early growth and lifecycle of galaxies, and hence, includes targets in a redshift range encompassing the peak of the star-formation epoch at $0.7 < z < 2.7$. KMOS^{3D} targets reside in the fields accessible to the VLT (GOODS-South, COSMOS and UDS) and are selected from the 3D-HST Treasury Survey (Brammer et al., 2012, for a description of these fields). Emission lines of interest are primarily Hα, [NII] and [SII], which are redshifted to fall in either the K, H or YJ band, according to Eq. 2.1. All galaxies have a magnitude $K < 23$. The wavelength range that each band covers is shown in Tab. 2.1.

2.3.2 Sample in this work

A subset of three galaxies from the nine galaxies for which a radial profile is available from W20 was selected to test the fitting routine developed in this work. HST images are available for all of them from the CANDELS survey (Grogin et al., 2011; Koekemoer et al., 2011) and are shown in Fig. 2.4. A table with their properties is also provided (Tab. 2.2). Names are adopted from the

KMOS^{3D} survey. GS4_12401 is a clear spiral galaxy with prominent arms, located in the GOODS-South field. U4_12959 and U4_19754 both reside in the UDS field. Of these galaxies, the first appears to have a quite irregular shape, with the possibility of a merger in-process. The latter appears to be more inclined with an inner concentration of light.

name	RA (J2000)	dec. (J2000)	z	i	θ
GS4_12401	3:32:52.87	-27:51:14.71	1.00175	20.8	-40
U4_12959	2:17:26.65	-5:14:00.45	1.03611	47.6	45
U4_19754	2:17:38.92	-5:12:37.10	1.46239	47.4	90

Table 2.2: Names in the KMOS^{3D} survey, coordinates (J2000), redshift, inclination and position angle of the subset of galaxies chosen for our test. Inclinations and position angles are in degrees. The acquisition of i and θ is explained in the text.

2.3.3 Fixed parameters

As explained in Sec. 2.2.1, the model requires several fixed input parameters which greatly impact the overall shape of the profile and thus the derived quantities. The parameters of interest are: inclination i, position angle θ, coordinates of the center (x_c, y_c), and the size of the PSF. However, W20 do not provide tabulated values for these parameters. Therefore, we try to reconstruct them as accurately as possible. The approaches for the inference of each parameter are described here.

W20 fitted HST F160W images with Sérsic models to infer i and θ, with initial guesses for the fit taken from the fits of van der Wel et al. (2014), who used GALFIT. However, some galaxies were not fitted by GALFIT. For these cases, initial guesses were taken from the SExtractor parameters obtained by Skelton et al. (2014), in particular the semi major ($A_{\rm img}$) and minor axis ($B_{\rm img}$) in the image in arcsec. For consistency, W20 then used empirical relations between SExtractor and GALFIT parameters to find the axis ratio q:

$$q = \frac{\sqrt{B_{\rm img}^2 - 0.15^2}}{\sqrt{A_{\rm img}^2 - 0.15^2}}, \tag{2.13}$$

where the term -0.15^2 comes from the derived empirical relation. SExtractor parameters are slightly rounder than those found by GALFIT (Holden et al., 2009). The ellipticity ϵ of a galaxy with axis ratio q is then given by:

$$\epsilon = 1 - q. \tag{2.14}$$

Instead of fitting HST images to infer θ and i, we adopt the SExtractor parameters $A_{\rm img}$ and $B_{\rm img}$ from Skelton et al. (2014) and use Eq. 2.13 to obtain the axis ratio. In turn, we use Eq. 2.14 to compute the ellipticity, which is used to find the inclination, according to (Dekel and Ostriker, 1999):

$$\cos^2 i = \begin{cases} \frac{(1-\epsilon)^2 - (1-\epsilon_{\rm max})^2}{1-(1-\epsilon_{\rm max})^2} & \epsilon < \epsilon_{\rm max} \\ 0 & \epsilon \geq \epsilon_{\rm max} \end{cases}, \tag{2.15}$$

where $\epsilon_{\rm max} = 0.8$ for an edge-on disk. The position angle θ is estimated from the HST images in Fig. 2.4. There is some uncertainty associated with these values when comparing best-fit models to those of W20, since their values were obtained with a Sérsic fit. Nevertheless, fitting HST images would still introduce an uncertainty as one cannot be sure that the fit is executed in

exactly the same fashion. Moreover, a rotation of a few degrees with respect to the 'true' value of θ has negligible to no impact on the final value for R_s.

A bigger point of concern is the celestial coordinates assigned to pixels in the data cubes. Errors in the astrometric registration of the objects result in shifts with respect to the true coordinates. The team at the VLT observatory periodically tweaks the positioning of KMOS arms to ensure that they remain within the required specifications. This leads to small variations in the calibration parameters, which ultimately cause the astrometric shifts (Wilman et al., 2020). Hence, we cannot directly use the central coordinates inferred from HST images (see crosses in Fig. 2.4). However, the location of the central point in our Hα maps can only be shifted in increments of 1 pixel unit (0.2″). This means that there is only a small number of feasible 'options' for the central pixel. After a few experiments, we adopted the pixels that produced the 1D profiles that best resembled the profiles from W20.

Next, the seeing conditions at the moment of observing can heavily influence galaxy size measurements, as demonstrated by Fig. 2.3. Therefore, it is important to include the correct size and shape of the PSF. Information about the PSF properties, including a PSF image and parameters for the best Gaussian and Moffat fit executed by Wisnioski et al. (2015), is stated in the fourth extension of the data cubes. W20 used the PSF image to convolve their functions. We resort to using the position angle, and FWHM major and minor axes from the Gaussian fit for all galaxies. In reality, the shape of the PSF might be more complicated than a Gaussian, which adds an unknown level of uncertainty to the fits. Regardless, the property of the PSF which most strongly affects the fit is its size, which is known.

Finally, W20 only fit data from pixels with at least 20 per cent of the nominal number of exposures for each galaxy. The KMOS^{3D} data cube headers contain information on the total number of combined exposures $N_{\rm exp}$. Additionally, an 'exposure map' $M_{\rm exp}(x, y)$ is provided in the second extension of the cubes, where the number of exposures for each pixel is stored. Instead of using a S/N threshold, we combine this information to create a mask $M_{\rm mask}(x, y)$ with fitting weights using the same criterion:

$$M_{\rm mask}(i,j) = \begin{cases} 1 & \text{if } M_{\rm exp}(i,j) \geq 0.2 N_{\rm exp} \\ 0 & \text{if } M_{\rm exp}(i,j) < 0.2 N_{\rm exp} \end{cases} , \tag{2.16}$$

such that only the pixels inside the mask are fitted. The final masks that are obtained using this criterion are shown in Fig. 2.5.

2.3.4 Results

In Fig. 2.5, the Hα maps, best-fit model functions, masks and residuals (map – model) for our test sample are displayed. The edges of the Hα maps (marked with dark green) are removed, because they contain extreme values, disrupting the color scale. The white ellipses in the first (left) panels indicate the annuli in which the surface brightness is extracted for the 1D radial profiles. They are aligned on the center, with inclination and position angle as explained in Sec. 2.3.3. The units of the map, model and residuals are 10^{-17} erg s^{-1} cm^{-2} arcsec^{-2}. In all cases, the residuals show regions where the model has a higher flux than the data and vice versa, demonstrating that the Hα distributions slightly deviate from an exponentially declining function. Regions with high Hα emission away from the center of the galaxy are smeared out as a result of the PSF, increasing the azimuthal asymmetry. However, we are only interested in radial differences. When the profiles are azimuthally averaged, the discrepancy between data and model is severely diminished (Fig. 2.6b). We go over the assessment of the radial profiles and inferred scale lengths in the next paragraph.

The inferred scale lengths from the best-fit models are given in Tab. 2.3. Uncertainties on inferred scale lengths are the statistical errors as explained in Sec. 2.2.1. Unreported errors

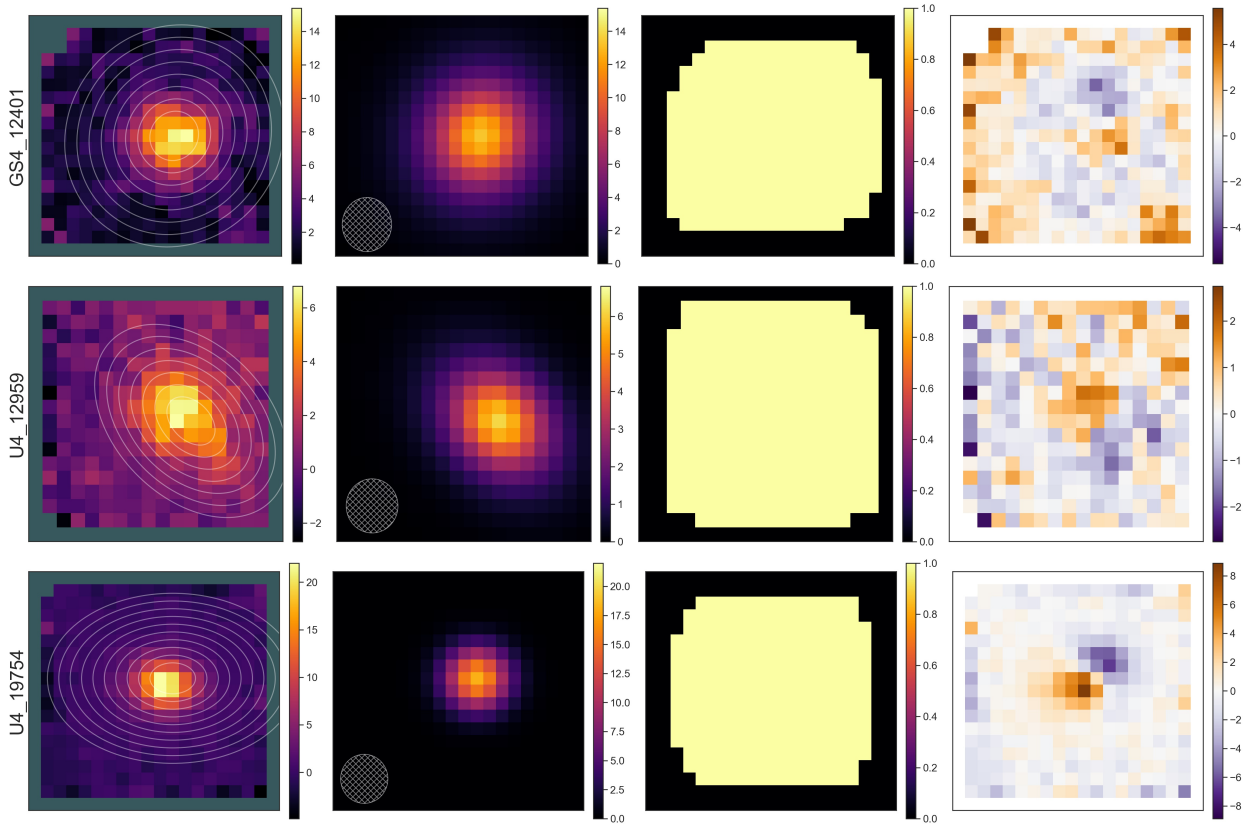

Figure 2.5: From left to right: first panel shows the Hα map $M_{\mathrm{H}\alpha}$(x,y) in units of 10^{-17} erg s^{-1} cm^{-2} arcsec^{-2} and the elliptical annuli (white ellipses) used to extract radial profiles. The data in the border pixels (marked dark green) are removed since they contain extreme values. Second panel shows the best-fit 2D exponential model convolved with the PSF in the same units. The hatched ellipse in the bottom left represents the shape of the PSF. Third panel shows the mask applied to the data in the fitting procedure. Pixels outside the yellow area are not fitted. Fourth panel shows the residuals of map – model, with the same units as the first and second panel.

are in the PSF, inclination i, position angle θ and coordinates of the center (x_c, y_c). These are not included because making a quantitative assessment on them is not as straightforward. As a consequence, our errors are likely underestimated. Half-light radii from W20, transformed to scale lengths using Eq. 1.3 are also given in the table. Radial profiles extracted from the Hα maps and best-fit model are shown in Fig. 2.6b. These profiles represent the mean flux calculated in elliptical annuli with the same inclination and position angle as used in the calculation of the best fit model. Since there is no uncertainty associated with the flux measured in each pixel, the error bars simply represent the statistical error in each annulus. The models are generally within or close to the error bars, showing that the models are in good agreement with the data when both are azimuthally averaged. The shaded grey area around the solid black line illustrates the shape of the profile using the minimum and maximum values of R_s, that is: $R_s \pm \sigma_{R_s}$. Although being relatively narrow at small r, the fact that its width increases with increasing r from the center demonstrates that the size of the scale length affects the overall shape of the profile more strongly in the outer regions. Fig. 2.6a demonstrates that the best-fit models from this work are in good agreement with the best-fit models from W20. The uncertainty in their profiles is obtained from generating bootstrap data cubes by randomly resampling channels. As mentioned in the previous sections, there is a substantial amount of fixed parameters for the model that could possibly differ from W20. Among them are the shape of the PSF, inclination and position angle, coordinates of

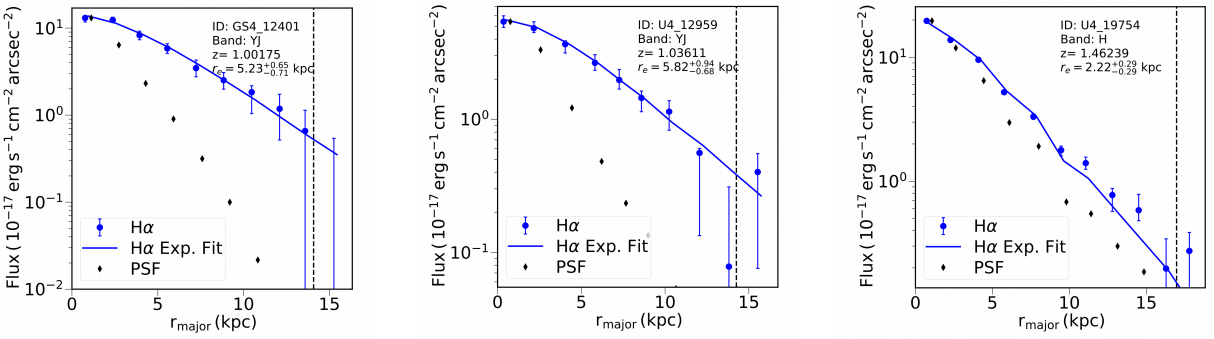

(a)

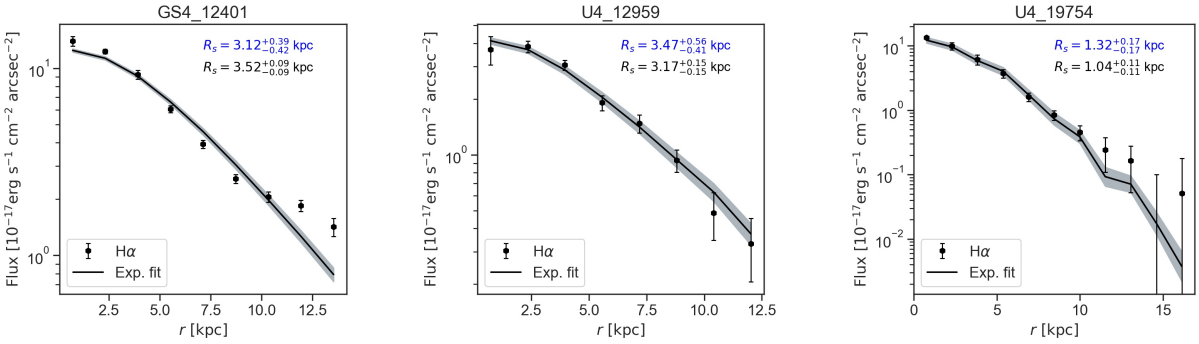

(b)

Figure 2.6: a) Radial profiles from Wilman et al. (2020) of the Hα maps (blue points with 1σ bootstrap errors) and best fit model (blue solid line). A PSF image is extracted in the same manner (black diamonds). The vertical dashed line indicates the radius where the major axis first crosses the edge of the KMOS field of view. **b)** Radial profiles extracted in elliptical annuli from our Hα maps (dots with error bars) and our best-fit exponential model (solid black line). The grey area is obtained by varying the fitted R_s by 1σ. The scale length from our best-fit model with errors is noted in black; the scale length from Wilman et al. (2020) is in blue.

the center, and even the Hα map itself, which is obtained with a different method. Nevertheless, in all cases the scale length we find agrees with the scale length from W20 within the 1σ uncertainty ranges. This leaves us to believe that our fitting routine is robust as it infers parameters that are consistent with the literature. We can then proceed to use it for our purposes in the next chapter.

galaxy	R_s	R_s **(W20)**
	kpc	kpc
GS4_12401	$3.52^{+0.09}_{-0.09}$	$3.12^{+0.39}_{-0.42}$
U4_12959	$3.17^{+0.15}_{-0.15}$	$3.47^{+0.56}_{-0.41}$
U4_19754	$1.04^{+0.11}_{-0.11}$	$1.32^{+0.17}_{-0.17}$

Table 2.3: The scale lengths found in this work and Wilman et al. (2020), indicated by W20.

Chapter 3

Sample and SFRD fitting

In this chapter, we define the adopted sample of $z \simeq 1$ galaxies from KROSS (Stott et al., 2016) and explain the acquisition of their properties. We also provide a description of the additional steps required to convert maps of Hα emission to maps of SFRD.

3.1 Sample description

3.1.1 KROSS survey

The KMOS Redshift One Spectroscopic Survey (KROSS) was designed to determine the dynamical state of galaxies at the peak of the star formation epoch (Stott et al., 2016). This program observed hundreds of spatially resolved galaxies at $z \simeq 1$, with the KMOS near-IR multi-integral-field-unit (IFU) spectrograph on the VLT (described in Sec. 2.1.1). The observed fields are UDS, ECDFS, COSMOS, SA22 (see Stott et al., 2016, for details of these fields and the spectroscopic or narrow-band surveys used for each galaxy). Observed targets encompass a redshift range of $z \simeq 0.8-1.0$, placing Hα in the YJ band (Tab. 2.1). The majority of galaxies are selected to have a magnitude $K_{AB} < 22.5$, corresponding to a stellar mass limit of $\log(M_*/M_\odot) = 9.3 \pm 0.5$. The sample was selected to satisfy several conditions: an integrated Hα flux of $F_{\mathrm{H}\alpha} > 5 \times 10^{-17}\,\mathrm{erg\,s^{-1}\,cm^{-2}}$ that assures a high S/N, an inclination in the interval $30° < i < 70°$ and a relatively wide stellar mass range of $2 \times 10^9\,\mathrm{M}_\odot - 5 \times 10^{10}\,\mathrm{M}_\odot$. Also, obvious mergers were excluded. Stott et al. (2016) report that their total sample of $z \simeq 1$ galaxies have on average higher velocity dispersions and are more gas-rich than their local counterparts, although the former of these results has been disputed by the subsequent study of Di Teodoro et al. (2016), who found Hα velocity dispersions comparable to those at $z \simeq 0$.

3.1.2 Sample in this work

Our sample consists of 12 galaxies from the KROSS survey, whose kinematics have been studied by Di Teodoro et al. (2016), and for which the Fall relation (Fall, 1983) has been investigated by Marasco et al. (2019). From the 18 galaxies analyzed in these studies, we exclude six galaxies: all galaxies (four) from the KMOS^{3D} survey, one galaxy that is cut-off in the bottom of the KMOS FOV, and a galaxy for which no Hα map is published by the KROSS team. Marasco et al. (2019) analyzed HST images of the sample, publishing stellar scale lengths which we adopt in our analysis. Their procedure is outlined in the following subsection. The total adopted sample in this work encompasses a redshift range of $z \simeq 0.84 - 1$. Average seeing conditions for each pointing are stated in Stott et al. (2016). For each galaxy, we adopt the average seeing in the respective field as the value for the FWHM in the calculation of the PSF. We assume a circular Gaussian PSF. Properties of our sample are reported in Tab. 3.1.

name	field	RA (J2000)	dec. (J2000)	z	log $M_*/M_\odot$	$F_{H\alpha}$	R_s	θ	i
		h m s	° ' "			10^{-17} esc*	kpc	°	°
C-HiZ_z1_195	COSMOS	10:00:34.63	+02:14:29.7	0.845	9.75 ± 0.09	6.52	1.9 ± 0.2	-10	49
C-HiZ_z1_258	COSMOS	00:01:05.65	+01:52:57.7	0.838	10.41 ± 0.11	5.52	4.4 ± 0.3	20	54
C-zcos_z1_192†	COSMOS	10:01:03.45	+01:54:00.4	0.914	10.17 ± 0.05	13.0	1.0 ± 1.0	-30	45
C-zcos_z1_202	COSMOS	10:00:53.39	+01:52:40.9	0.841	10.54 ± 0.06	35.1	2.2 ± 0.1	20	45
C-zcos_z1_690	COSMOS	10:00:36.55	+02:13:09.5	0.925	10.69 ± 0.25	8.69	2.4 ± 0.1	80	50
C-zcos_z1_692	COSMOS	10:00:36.42	+02:11:19.2	0.927	10.61 ± 0.18	18.9	3.1 ± 0.2	45	42
E-zmus_z1_21	GOODS-S	03:32:48.48	-27:54:16.0	0.839	10.40 ± 0.14	6.79	3.3 ± 0.2	90	32
E-zmus_z1_119	GOODS-S	03:32:08.20	-27:47:52.1	0.841	10.34 ± 0.07	10.3	3.3 ± 0.2	30	62
E-zmus_z1_125	GOODS-S	03:32:21.76	-27:47:24.7	0.998	9.95 ± 0.06	5.06	1.7 ± 0.1	85	58
E-zmus_z1_129	GOODS-S	03:32:26.29	-27:47:17.5	0.995	9.83 ± 0.07	6.14	2.3 ± 0.1	-45	43
E-zmus_z1_166	GOODS-S	03:32:16.49	-27:44:49.0	0.875	10.11 ± 0.15	10.5	2.0 ± 0.1	-85	51
E-zmus_z1_217†	GOODS-S	03:32:20.53	-27:40:58.8	0.894	10.02 ± 0.08	6.75	4.0 ± 0.2	50	70

Table 3.1: Properties of adopted galaxy sample. Geometrical parameters (position angle and inclination) are from Di Teodoro et al. (2016). Stellar masses are adopted from Santini et al. (2015). Redshifts and Hα fluxes are obtained from Harrison et al. (2017). Scale lengths and coordinates of the center are from Marasco et al. (2019).
† Galaxies excluded from the final analysis (explained in Sec. 3.2.2).
* erg s^{-1} cm^{-2}.

Scale length

Marasco et al. (2019) used Hubble Space Telescope (HST) Wide Field Camera 3 (WFC3) images in two bands as a probe for the stellar distribution. In a similar fashion to the technique outlined in Sec. 1.3.3, they fit an exponentially declining function of the form $f(R) = K \exp\left(-\frac{R}{R_*}\right)$ to obtain scale lengths of their galaxy sample. However, instead of fitting 2D maps, they fit the function on radial profiles, extracted from the images by calculating the surface brightness in elliptical annuli. Since the HST resolution is very high, galaxies are well-resolved, such that it becomes unnecessary to account for the PSF. The used bands are F160W and F814W, which have mean wavelengths λ_{mean} of 15 337 Å and 8133 Å, respectively. From Eq. 2.1, we find that the rest-frame mean wavelength of the F160W band is $\lambda \approx 7600$ Å at $z = 1$, which is in the red side of the optical spectrum. Adopted scale lengths in this thesis used for informing the SFRD model are the fitted value from Marasco et al. (2019) in the F160W band, as it is, among the two, the least affected by dust extinction and therefore a more reliable tracer of the SMSD as explained in Sec. 1.3.1. Fig. 3.1 presents an example of the radial profile extraction and exponential fit on the resulting profile.

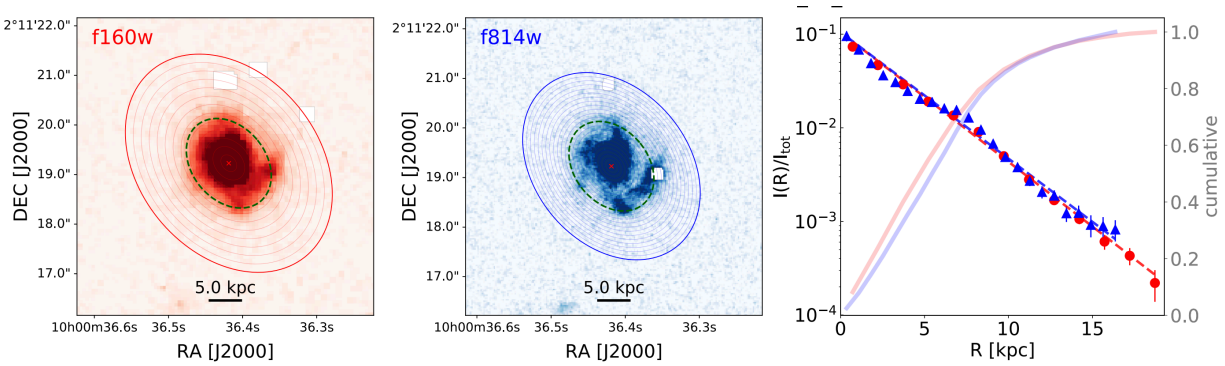

Figure 3.1: Figure taken from Marasco et al. (2019) showing the extraction of radial profiles for the galaxy C-zcos_z1_692 in bands F160W and F814W. The right panel is a plot of the surface brightness as a function of radius (see elliptical annuli in the left and middle panels), normalized to the total surface brightness enclosed in the largest ellipse. Red circles are used for the F160W image (left panel); blue triangles are used for the F841W image (middle panel). Dotted lines represent the best-fit exponential function for $R > 3.5$ kpc. Solid lines are the cumulative light profiles. The stellar mass radial profile nearly perfectly follows an exponential.

3.2 Creation and centering of Hα maps

3.2.1 Rebinning

In contrast to the KMOS spatial pixel scale of $0.2'' \times 0.2''$, KROSS data cubes are binned to a spatial scale of $0.1'' \times 0.1''$, which allowed the KROSS team to improve the cube mosaics using sub-pixel shifts. Likewise, the KROSS team have published Hα maps for their targets using this spatial scale. These maps have an artificially increased spatial resolution by means of interpolation, which quadruples the amount of pixels in the image. We opted not to use these maps in our analysis of the SFRD for two main reasons: 1) these maps often inherit errors, with some containing oversaturated pixels more than 100 times the mean value of the map, and 2) the fact that their spatial resolution is artificially enhanced means that they are prone to an added uncertainty due to the interpolation between pixels. However, we use these maps to correct our maps for the astrometric error. This procedure is described in Sec. 3.2.2. We extract Hα maps from the data cubes using the same procedure as described in 2.1.2 and rebin our final Hα maps to the original KMOS pixel scale of $0.2'' \times 0.2''$.

3.2.2 Re-centering of maps

As explained in Sec. 2.3.3, there are some errors in the astrometric registration of the KMOS data cubes. In most cases, this results in a small shift ($\sim 0.2'' - 0.4''$) w.r.t. the true coordinates. The KROSS team used the continuum emission in the band to relocate the center of the galaxy. By stacking all channels in the data cube without emission lines, a map of the continuum emission in the YJ band can be obtained. The emission in these continuum maps is expected to be comparable (although at much lower spatial resolution) to the emission in the HST F160W filter. In such filters, these galaxies have their centers located at the (or very close to) the brightest pixel. Thus, if the pixel with the highest intensity can be identified in the KMOS continuum maps, this will indicate the position of the center of the galaxy. The shift from the center in this continuum map w.r.t. the center in HST continuum images can subsequently be used to infer the correct location of the center in the Hα map. Published Hα maps by the KROSS team have been re-centered using this technique. Important to note is, however, that the continuum emission is very weak in the KMOS data cubes. This makes the application of the technique diffult for some galaxies

and it could result in incorrect re-centering. In our analysis, we adopt the same shift as the one inferred by KROSS for consistency. We do this by using the re-centered images from KROSS to infer the correct positioning of our maps. The astronomical imaging and data visualization application SAOIMAGEDS9 (Joye and Mandel, 2003) was used for this process. By matching the coordinates of our map in frame 1 with the coordinates of the KROSS map in frame 2 and plotting contours of our map as an overlay in frame 2, the vertical and horizontal shift can be inferred. An example of galaxy E-zmus_z1_125, which requires a relatively large correction, is shown in Fig. 3.2. However, we have reasons to doubt that the re-centering is correct for two galaxies (C-zcos_z1_192 and E-zmus_z1_217), as the process results in centers that are severely misaligned with the Hα distribution (Fig. 3.3). Moreover, the shape of the Hα emission appears similar (but offset) to that of the stellar emission (white ellipses in left panel of Fig. 3.3). These galaxies are therefore excluded from the analysis.

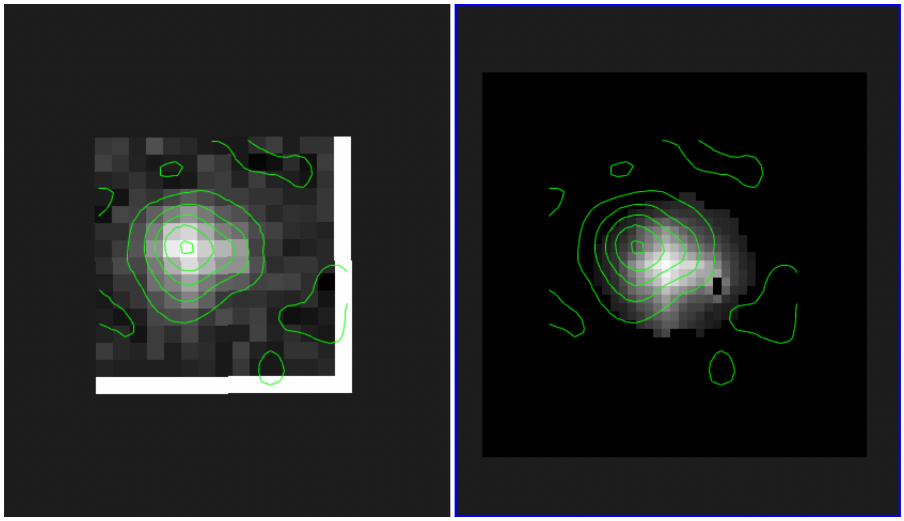

Figure 3.2: Example of galaxy E-zmus_z1_125 demonstrating how the contour overlay function in SAOIMAGEDS9 (Joye and Mandel, 2003) was used to re-center the Hα maps of the sample. Green contours from the Hα map on the left are overplotted on the KROSS map (right) of the same galaxy. The shift that is needed to overlay the two maps is evident.

3.2.3 Unit conversion

The KROSS data products do not specify units. Therefore, we have to re-normalize our maps using the Hα flux $F_{\mathrm{H}\alpha}$, such that they are in units of surface brightness $\mathrm{SB}_{\mathrm{H}\alpha}$ [erg s^{-1} cm^{-2} arcsec^{-2}]. Including the unit of arcsec^{-2} allows for a conversion to SFR *surface density* later in the process. We do this by finding coefficient A with units of $\mathrm{SB}_{\mathrm{H}\alpha}$, which, when multiplied by the total flux density in our map, gives us $F_{\mathrm{H}\alpha}$. Each pixel in our Hα map has a value v_i, and a size of 0.04 arcsec^2, such that the flux density in that pixel is given by:

$$F_i\ [\mathrm{erg\,s^{-1}\,cm^{-2}}] = v_i \times A\ [\mathrm{erg\,s^{-1}\,cm^{-2}\,arcsec^{-2}}] \times 0.04\ \mathrm{arcsec^2}. \tag{3.1}$$

From this follows that the total flux density of the galaxy $F_{\mathrm{H}\alpha}$ is given by the sum of fluxes in each pixel:

$$F_{\mathrm{H}\alpha} = \sum_i F_i = 0.04 \sum_i v_i \times A\ [\mathrm{erg\,s^{-1}\,cm^{-2}}], \tag{3.2}$$

such that A is obtained by:

$$A = \frac{F_{\mathrm{H}\alpha}}{0.04 \sum_i v_i}. \tag{3.3}$$

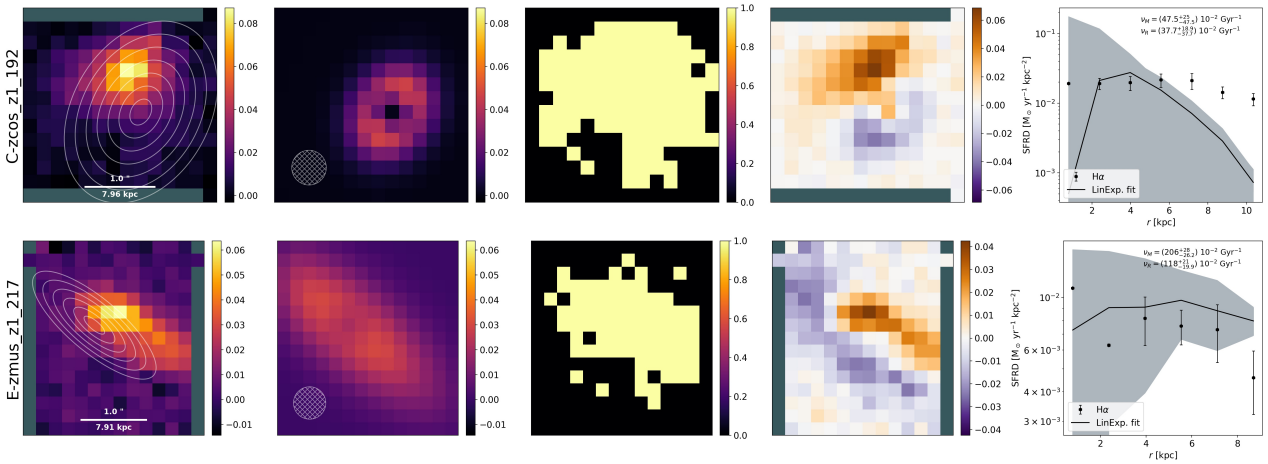

Figure 3.3: From left to right: SFRD map, 'best-fit' SFRD model, mask, residuals (map – model) and 1D radial profile of galaxies C-zcos_z1_192 (top) and E-zmus_z1_217 (bottom). Units of all panels except the mask are $M_\odot\,yr^{-1}\,kpc^{-2}$. The hatched circle in the second panels indicates the shape of the PSF. The white ellipses in the left panel are the annuli used for the extraction of radial profiles. The various panels of this figure and in particular the right panel, are described in more detail in Chapter 4.

Multiplying our maps by A gives units of $SB_{H\alpha}$ [$erg\,s^{-1}\,cm^{-2}\,arcsec^{-2}$]. In Sec. 3.3 we explain how these maps can then be converted to maps of SFRD.

3.2.4 Mask

The KMOS data and resulting Hα maps can contain significant noise levels. Therefore, we determine which pixels contain trustworthy emission for the fitting routine by setting a S/N threshold. We opted for a fiducial value (i.e. holding for all galaxies) of 1.5. Using this threshold, a mask is created as described in Sec. 2.2.2. This means that only pixels with emission larger than 1.5 times the noise in the image are fitted. The value of 1.5 was chosen after experimenting with different values, as this resulted in the best overall account for the visual distribution of Hα emission in all maps. To estimate the noise, each map is examined individually to find the rows and columns of pixels that are not contaminated by emission from the galaxy. Generally this resulted in the first to third upper and lower rows, and/or first to third outer-left and outer-right columns. The noise is attained by computing the standard deviation in these rows and/or columns of pixels. The impact that our choice for the S/N threshold has on our final results are discussed in Sec. 4.4.

3.3 Conversion of Hα surface brightness to SFRD

In this section, the applied techniques for converting our Hα maps to units of SFRD are described. We start by using the relation from Kennicutt and Evans (2012) to connect the total Hα luminosity to SFR:

$$\mathrm{SFR}\,[M_\odot\,yr^{-1}] = 5.37\times10^{-42}\;L_{H\alpha}\,[erg\,s^{-1}], \tag{3.4}$$

which is the same as Eq. 1.4, but in linear space. The SFRD is then obtained by dividing the SFR of a considered region by its surface area A:

$$\mathrm{SFRD}\,[M_\odot\,yr^{-1}\,cm^{-2}] = \frac{\mathrm{SFR}}{A} = \frac{5.37\times10^{-42}\;L_{H\alpha}\,[erg\,s^{-1}]}{A\,[cm^2]}. \tag{3.5}$$

The angular diameter distance d_A relates the area A to the solid angle $\mathrm{d}\Omega$ with dimensionless units of sr:

$$\mathrm{d}\Omega = \frac{A}{d_A^2}. \tag{3.6}$$

The luminosity in Eq. 3.5 can be rewritten in terms of flux:

$$L_{\mathrm{H}\alpha}\,[\mathrm{erg\,s^{-1}}] = 4\pi d_L^2 \times F_{\mathrm{H}\alpha}\,[\mathrm{erg\,s^{-1}\,cm^{-2}}], \tag{3.7}$$

where d_L is the luminosity distance in cm. Combining the information from Eq. 3.6 and Eq. 3.7 gives a new definition for the SFRD:

$$\mathrm{SFRD}\,[\mathrm{M_\odot\,yr^{-1}\,cm^{-2}}] = \frac{5.37\times10^{-42}\times 4\pi d_L^2 \times F_{\mathrm{H}\alpha}\,[\mathrm{erg\,s^{-1}\,cm^{-2}}]}{\mathrm{d}\Omega \times d_A^2}, \tag{3.8}$$

where both the angular diameter distance d_A and luminosity distance d_L are in cm. There exists a relation between these quantities, involving redshift z:

$$d_L = (1+z)^2 d_A, \tag{3.9}$$

such that Eq. 3.8 simplifies to:

$$\mathrm{SFRD}\,[\mathrm{M_\odot\,yr^{-1}\,cm^{-2}}] = 6.75\times10^{-41}\ \frac{F_{\mathrm{H}\alpha}\,[\mathrm{erg\,s^{-1}\,cm^{-2}}]}{\mathrm{d}\Omega}\,(1+z)^4, \tag{3.10}$$

where the factor 4π has been included in the first coefficient. Dividing $F_{\mathrm{H}\alpha}$ by the solid angle leaves us with the surface brightness $\mathrm{SB}_{\mathrm{H}\alpha}$ in terms of $\mathrm{erg\,s^{-1}\,cm^{-2}\,sr^{-1}}$. We can therefore write our SFRD as follows:

$$\mathrm{SFRD}\,[\mathrm{M_\odot\,yr^{-1}\,cm^{-2}}] = 6.75\times10^{-41}\ (1+z)^4\ \mathrm{SB}_{\mathrm{H}\alpha}\,[\mathrm{erg\,s^{-1}\,cm^{-2}\,sr^{-1}}]. \tag{3.11}$$

Furthermore, $1\,\mathrm{sr} = 4.25\times10^{10}\,\mathrm{arcsec^2}$ and finally, we convert the SFRD units of $\mathrm{cm^{-2}}$ to $\mathrm{kpc^{-2}}$ to obtain:

$$\mathrm{SFRD}\,[\mathrm{M_\odot\,yr^{-1}\,kpc^{-2}}] = 2.73\times10^{13}\ (1+z)^4\ \mathrm{SB}_{\mathrm{H}\alpha}\,[\mathrm{erg\,s^{-1}\,cm^{-2}\,arcsec^{-2}}]. \tag{3.12}$$

Eq. 3.12 is used to convert our maps in terms of $\mathrm{SB}_{\mathrm{H}\alpha}$ to SFRD. Finally, the maps are multiplied by a factor $(1-\mathscr{R})$, such that they take into account the return fraction: the reduced SFRD (1.3.3).

Chapter 4

Results and discussion

Having constructed our SFRD maps as described in Chapter 3, we then follow the same fitting procedure as in Chapter 2, but except that now, instead of fitting an exponential function, we fit the SFRD model (Eq. 1.6), convolved with a Gaussian PSF and using ν_M and ν_R as free parameters. The parameters M_* and R_s are included in the set of fixed parameters depending on the galaxy as these are known from previous studies, as explained in Sec. 3.1.2. The fitting routine is executed to find best-fits, allowing us to infer ν_M and ν_R for our sample.

4.1 Best-fit models

Our final SFRD maps, best-fit SFRD models, masks, residuals, and 1D radial profiles are shown in Fig. 4.1. The shaded grey area surrounding the extracted 1D radial profile of the best-fit SFRD model (solid black line) is obtained by considering all models with parameters in the range $\nu_M \pm \sigma_{\nu_M}$ and $\nu_R \pm \sigma_{\nu_R}$, such that this area covers the model's total range of possible SFRD values within the uncertainties of ν_M and ν_R. The fitting routine reports statistical errors for all fitted parameters (as explained in Sec. 2.2.2). However, we should also include the uncertainty in the scale length, which impacts uncertainties on growth rates. The upper and lower levels of uncertainty in growth rates are obtained from executing the fit an additional two times: with $R_s \pm \sigma_{R_s}$ using the values reported in Marasco et al. (2019). These fits produce new values: ν_M^+, ν_M^-, ν_R^+ and ν_R^-, and their associated statistical uncertainties. The upper uncertainty level in ν_M is defined as the maximum value of either its statistical uncertainty σ_{ν_M}, or the difference between ν_M and ν_M^+, including the statistical error in ν_M^+. The same holds for the lower uncertainty level in ν_M and upper and lower uncertainty levels in ν_R. In general, this can be expressed as follows:

$$\sigma_\nu^{\text{upper}} = \max\left[\sigma_\nu,\ U^+\right], \tag{4.1}$$

$$\sigma_\nu^{\text{lower}} = \max\left[\sigma_\nu,\ U^-\right], \tag{4.2}$$

$$\text{with} \quad U^\pm = |\nu - (\nu^\pm \pm \sigma_{\nu^\pm})|$$

It evident that most galaxies leave systematic patterns of over- and underdensities in their residual maps. Such patterns are most likely due to off-centered star formation (Hα emitting) regions, which are common in $z \simeq 1$ galaxies (e.g. Nelson et al., 2012; Mieda et al., 2016). The severity of this effect may also be enhanced by the influence of the PSF, as explained in 2.3.4. Alternatively, in some cases it is also possible that the re-centering executed by KROSS may not have been completely accurate as a result of the faint continuum. Not all residual maps display such features: for some galaxies the residual map does not contain clear patterns, such that the SFRD map is well-represented by the axisymmetric model. However, the 1D radial profiles reveal that all azimuthally averaged maps and models are in good agreement. There is one case (galaxy C-HiZ_z1_258) where the SFRD shows an inner depression, due to an Hα region away from the

center. This feature is not reproduced by the best-fit model, but the data and model are within their respective uncertainties.

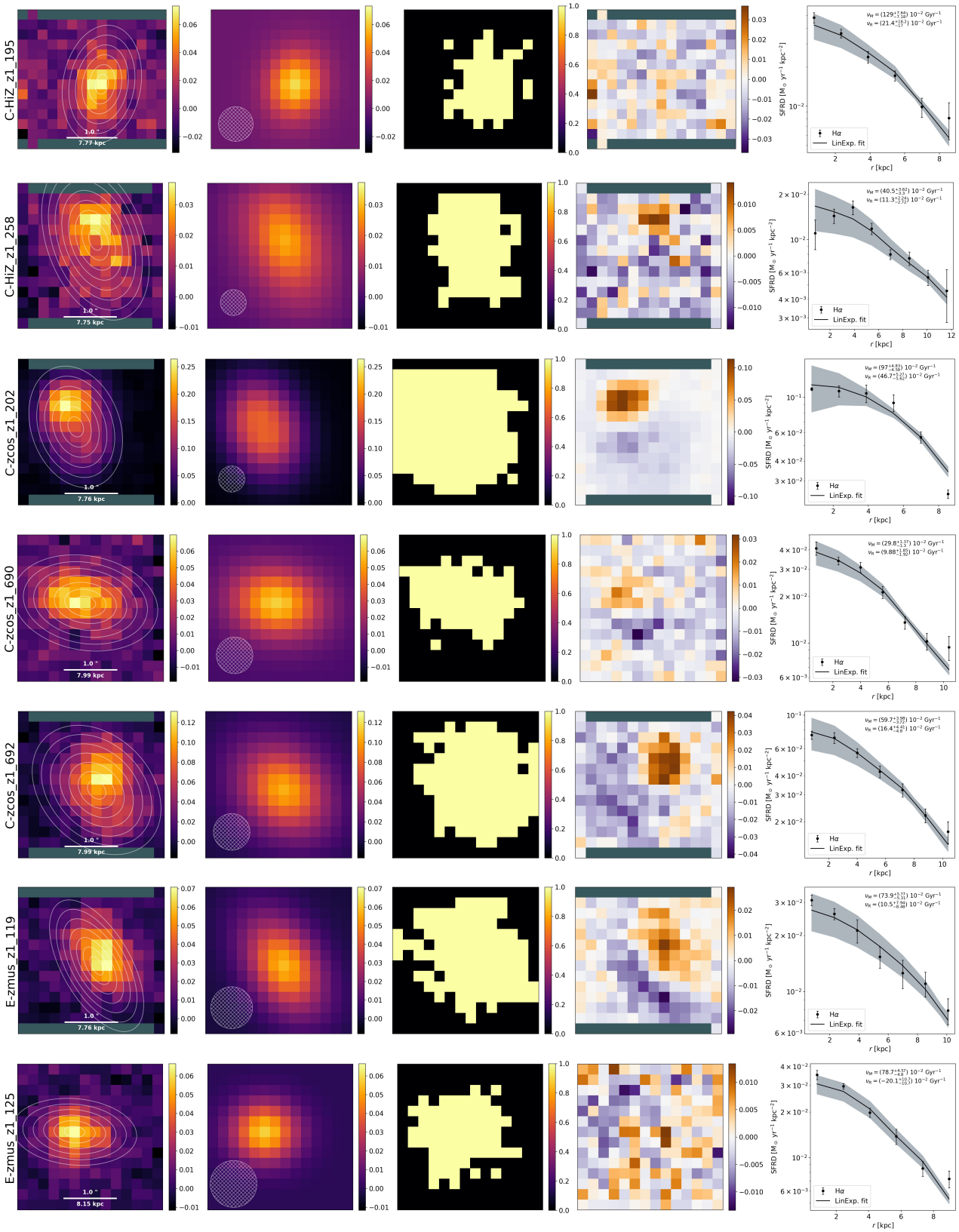

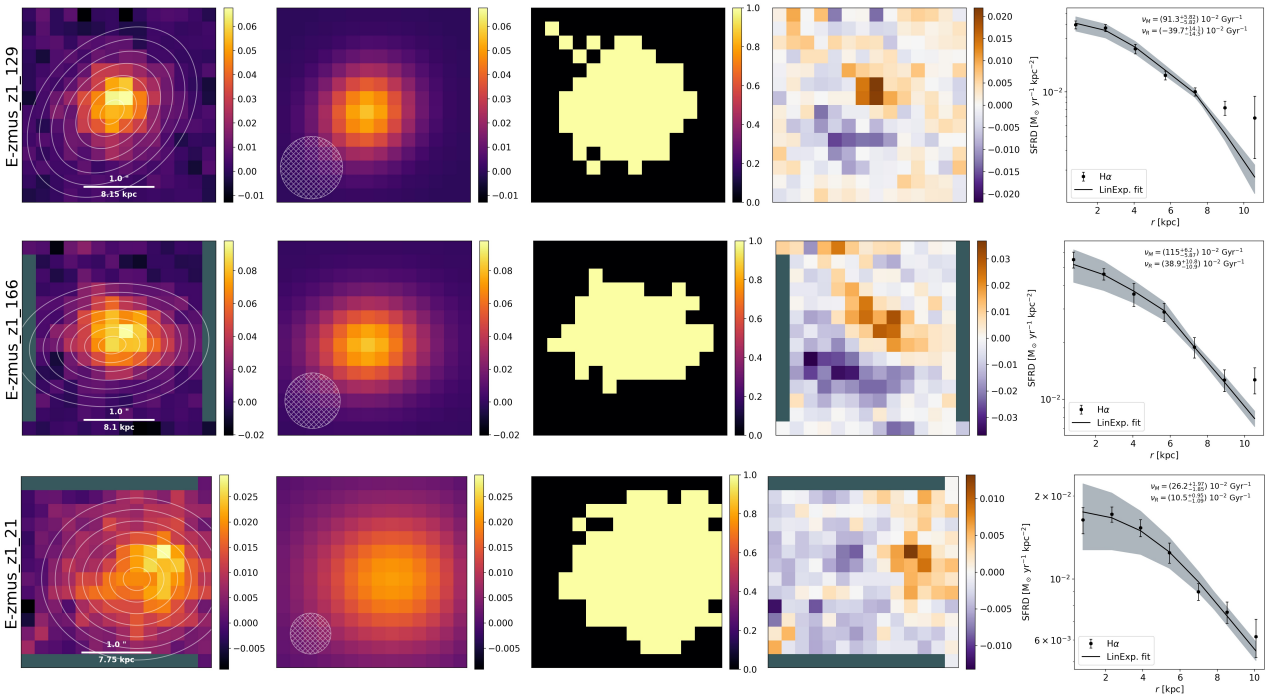

Figure 4.1: From left to right: first panel shows the SFRD map in units of $M_\odot\,yr^{-1}\,kpc^{-2}$. Blank values in the data are marked with dark green. The white ellipses are the elliptical annuli used for the extraction of radial profiles, centered on the center coordinates of the galaxy and with the same θ and i as used for the fixed parameters of the 2D model. Second panel shows the best-fit SFRD model, in the same units as the first panel. The hatched circle in the bottom-left corner of this panel shows the size and shape of the PSF. Third panel shows the mask applied during the fitting routine. Pixels outside the yellow area (S/N $<$ 1.5) are not fitted. Fourth panel shows the residuals of observed map – model, in the same units as the first panel. Fifth panel displays the extracted 1D radial profiles of the data (points with error bars) and model (solid line). Error bars of the data are statistical variations in each annulus. The shaded grey area is obtained by varying the SFRD model by $\nu_M \pm \sigma_{\nu_M}$ and $\nu_R \pm \sigma_{\nu_R}$. The best-fit parameters are indicated in the fifth panel.

4.2 Mass and radial growth rates

Tab. 4.1 lists the specific mass and radial growth rates of the sample inferred from the best-fit SFRD models. In Fig. 4.2, the specific mass and radial growth rates are plotted versus stellar mass and scale length of the disks. Statistics of the sample are stated in Tab. 4.2.

4.2.1 Mass growth rates

We find that our mass growth rates take a relatively narrow range of values, with a total spread of approximately 0.8 dex in logarithmic units (Fig. 4.2). The total scatter[1] is 0.357 Gyr^{-1} or 0.23 dex. To visualize and quantitatively compare the results for the mass growth rate of our sample with the literature, we plot the mass growth rate versus stellar mass (4.2, top-left panel). Studies have revealed (Speagle et al., 2014, provide a summary) that there is a strong correlation between SFR and M_* at fixed redshifts (the main sequence of star-forming galaxies), generally of the form:

$$\log \mathrm{SFR} = \alpha \log M_* + \beta \tag{4.3}$$

$$\log \mathrm{sSFR} = (\alpha - 1) \log M_* + \beta, \tag{4.4}$$

[1] The scatter is calculated as the standard deviation around the mean.

galaxy	ν_M	ν_R
	10^{-2} Gyr^{-1}	10^{-2} Gyr^{-1}
C-HiZ_z1_195	$129.1^{+7.64}_{-7.18}$	$21.41^{+16.2}_{-17.0}$
C-HiZ_z1_258	$40.54^{+3.62}_{-3.30}$	$11.28^{+2.24}_{-2.72}$
C-zcos_z1_202	$96.97^{+4.83}_{-4.69}$	$46.96^{+5.27}_{-5.62}$
C-zcos_z1_690	$29.78^{+1.37}_{-1.30}$	$9.879^{+1.85}_{-1.92}$
C-zcos_z1_692	$59.74^{+3.98}_{-3.72}$	$16.41^{+4.41}_{-4.80}$
E-zmus_z1_21	$26.16^{+1.97}_{-1.84}$	$10.52^{+0.95}_{-1.09}$
E-zmus_z1_119	$73.93^{+5.77}_{-5.31}$	$10.47^{+7.94}_{-8.48}$
E-zmus_z1_125	$78.67^{+4.57}_{-4.80}$	$-20.12^{+10.7}_{-10.7}$
E-zmus_z1_129	$91.26^{+5.82}_{-5.82}$	$-39.69^{+14.1}_{-14.5}$
E-zmus_z1_166	$115.1^{+6.20}_{-5.87}$	$38.92^{+10.8}_{-10.9}$

Table 4.1: The specific mass and radial growth rates of our sample.

	$\nu_R > 0$	all
ν_M/Gyr^{-1}		
median	0.668	0.763
scatter	0.367	0.334
ν_R/Gyr^{-1}		
median	0.138	0.109
scatter	0.134	0.239

Table 4.2: Statistics of specific mass and radial growth rates.

where the second equation expresses the same relation, but for the *specific* SFR (sSFR $\equiv \dot{M}_*/M_*$). Reminding that ν_M is the reduced specific star formation rate of the disk, we should observe a somewhat similar trend. The SFR – M_* relation for $z \simeq 1$ galaxies in a similar mass range, found by Elbaz et al. (2007), is plotted in the upper left panel of Fig. 4.2 (green line). It is shifted by $\log(1-\mathscr{R}) = \log(1-0.3)$, so as to make it comparable to our reduced sSFR. The shaded area indicates the 0.21 dex scatter around the relation. It is evident that our measured values of the reduced sSFR are in good agreement with the relation, although carrying a slightly larger scatter than the relation would suggest. We stress that reduced specific SFRs (ν_M) in this work were determined using our SFRD model, which is a very different method than what is usually employed for the sSFR. This agreement with the literature is important and therefore a non-trivial validation of our adopted methodology.

There appears to be an inverse trend for mass growth rate with scale length that can be inferred from the top-right panel in 4.2. However, this is uncertain due to the limited sample size. The two galaxies with the largest mass growth rate are amongst the most compact (smallest R_s) galaxies in

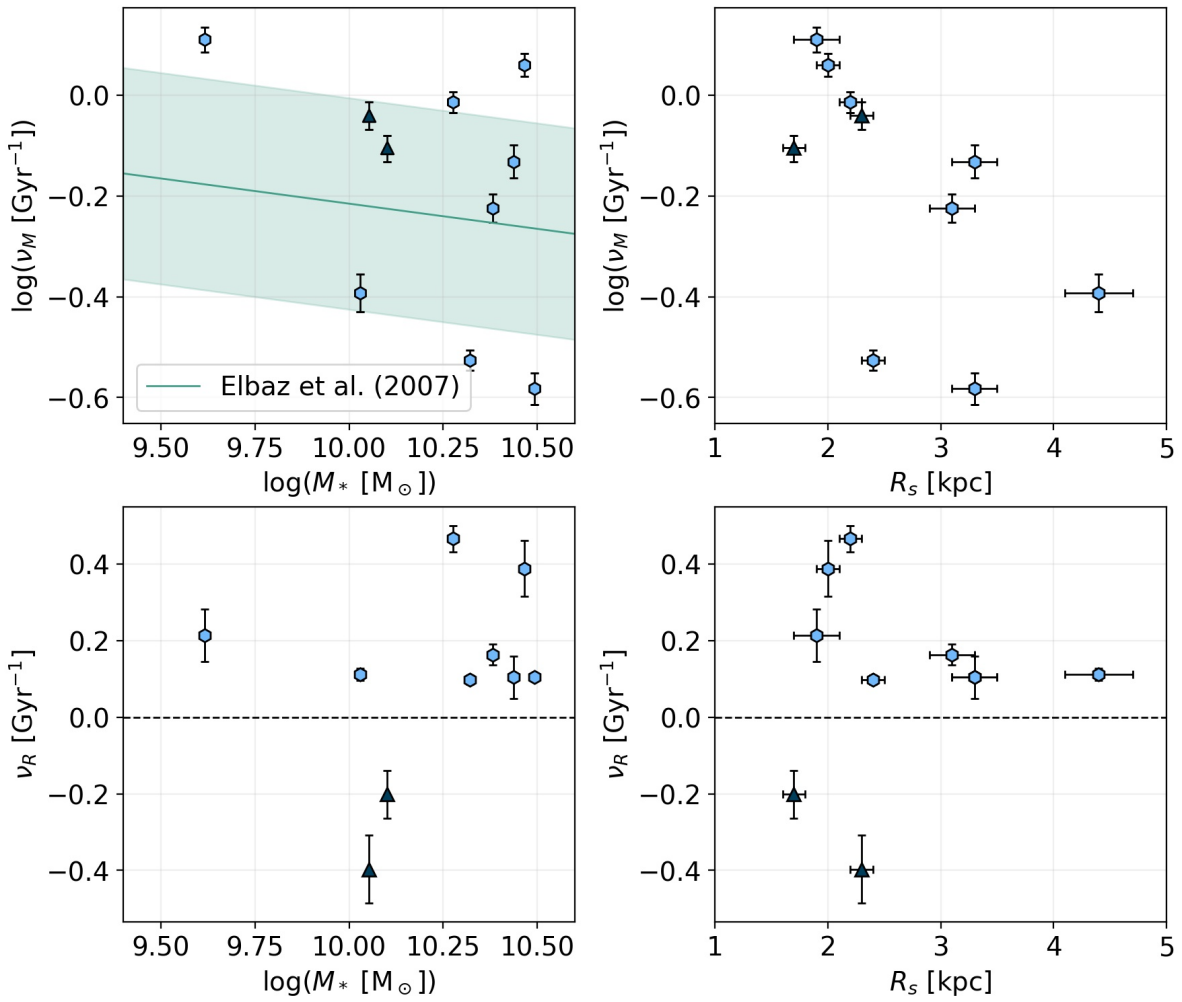

Figure 4.2: Specific mass (*top*) and radial (*bottom*) growth rates versus stellar mass (*left*) and scale length (*right*) of the final sample. The radial growth rates are not in logarithmic scale since two galaxies have negative values. These galaxies are indicated with the dark blue triangles in all panels. The green line in the top-left panel indicates the sSFR – M_* relation from Elbaz et al. (2007) shifted by $\log(1-\mathcal{R})$, with the shaded area marking its scatter of 0.21 dex. The black dashed lines in the bottom panels show the $\nu_R = 0$ boundary.

the sample, and the largest (R_s) galaxies have low to intermediate ν_M. The median mass growth rate of the inside-out growing galaxies in the sample is a factor ~ 7.5 larger than the median found by P15, indicating that galaxy disks at $z \simeq 1$ grow their mass ~ 7.5 times faster than their Local Universe counterparts. This corresponds to a rough estimate for the mass growth timescale of ~ 1.3 Gyr at $z \simeq 1$.

4.2.2 Radial growth rates

Of our final sample of 10 galaxies, we find that 80% exhibit inside-out growth ($\nu_R > 0$). The two galaxies that show signs of outside-in growth have significantly negative radial growth rates. In Fig. 4.2, these galaxies are indicated with the dark blue triangles. From the plots we see that they are relatively small ($R_s \sim 2$ kpc), but have intermediate stellar masses ($M_* \sim 10^{10}$ M$_\odot$). If we examine these cases individually, it becomes clear that both galaxies display some peculiarities. Starting with the galaxy showing the largest negative radial growth rate, E-zmus_z1_129, its radial profile in the F814W continuum image shows a bump near the center compared to its

profile in the F160W band (Marasco et al., 2019), shown in Fig. 4.3. At this redshift, the emitted light in the F814W band is in the blue part of the visible spectrum. The fact that this galaxy shows an increase in surface brightness towards the center in that band may indicate enhanced star formation in the center. A possibility could be that the galaxy has recently undergone a merger (triggering central star formation). This argument is further supported by its asymmetrical shape, in particular a large spiral arm feature that is visible on the south-east of the HST images in both bands. The other galaxy with negative radial growth rate, E-zmus_z1_125, also shows an extended spiral arm on one side, but it shows a small depression in the central regions in both the F814W and F160W surface brightness profiles (Fig. 4.3). From the HST images it becomes apparent that there is another galaxy (masked) within a $\sim 1''$ projected distance from its center. However, the fact that this galaxy does not show up in the Hα data cube suggests that it is not at the same redshift. Since 8/10 galaxies show significant radial growth, and only two are significantly shrinking, we find that our results are consistent with the general picture of inside-out growth of galaxies at $z \simeq 1$.

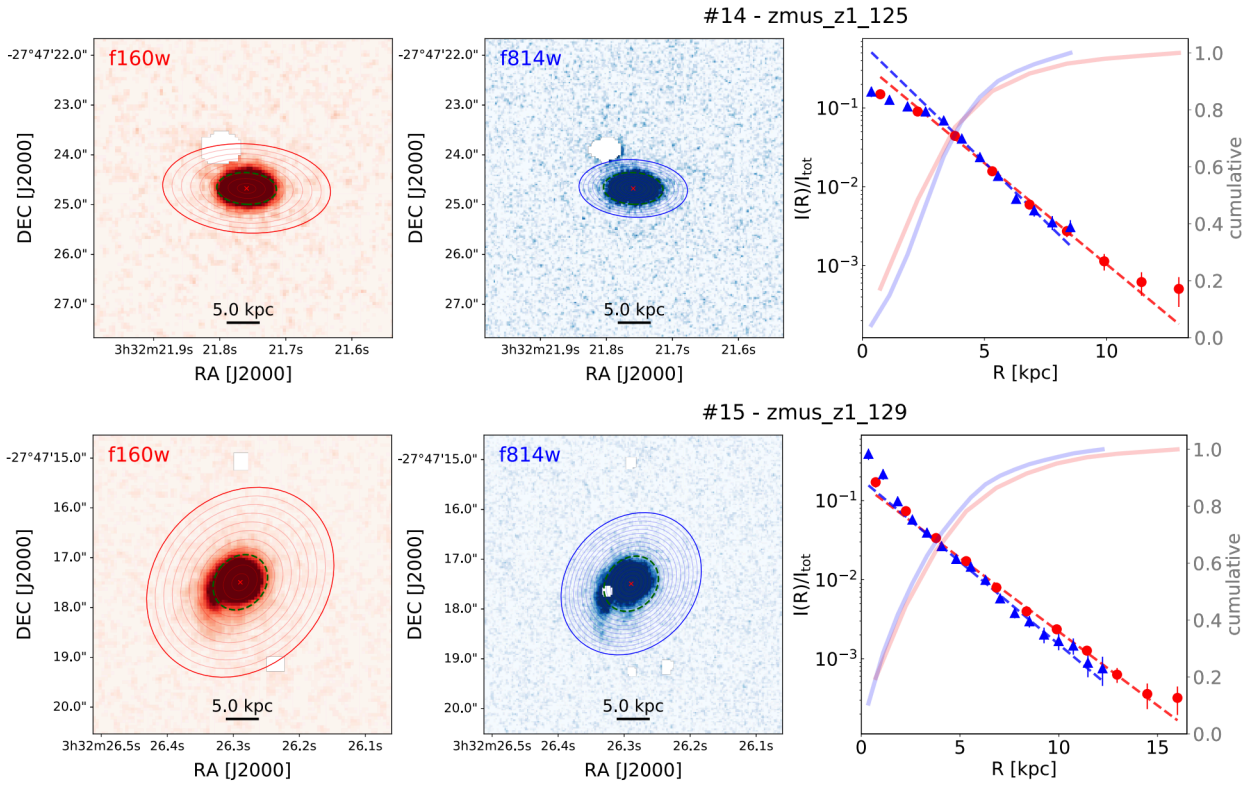

Figure 4.3: Same as Fig. 3.1, but for galaxies E-zmus_z1_125 and E-zmus_z1_129. Figure taken from Marasco et al. (2019).

There seems to be no strong trend in ν_R versus R_s that can be derived from the plot in the bottom-right panel of Fig. 4.2. The trend in radial growth rates versus stellar mass (bottom-left panel) seems to be relatively constant. The median of our positive radial growth rates is ~ 4.8 smaller than the median of the mass growth rates of inside-out growing galaxies. Furthermore, the median radial growth rate of our sample is ~ 7 times larger than radial growth rates at $z \simeq 0$ found by P15, which shows that $z \simeq 1$ galaxies grow ~ 7 times faster in radius than galaxies in the Local Universe.

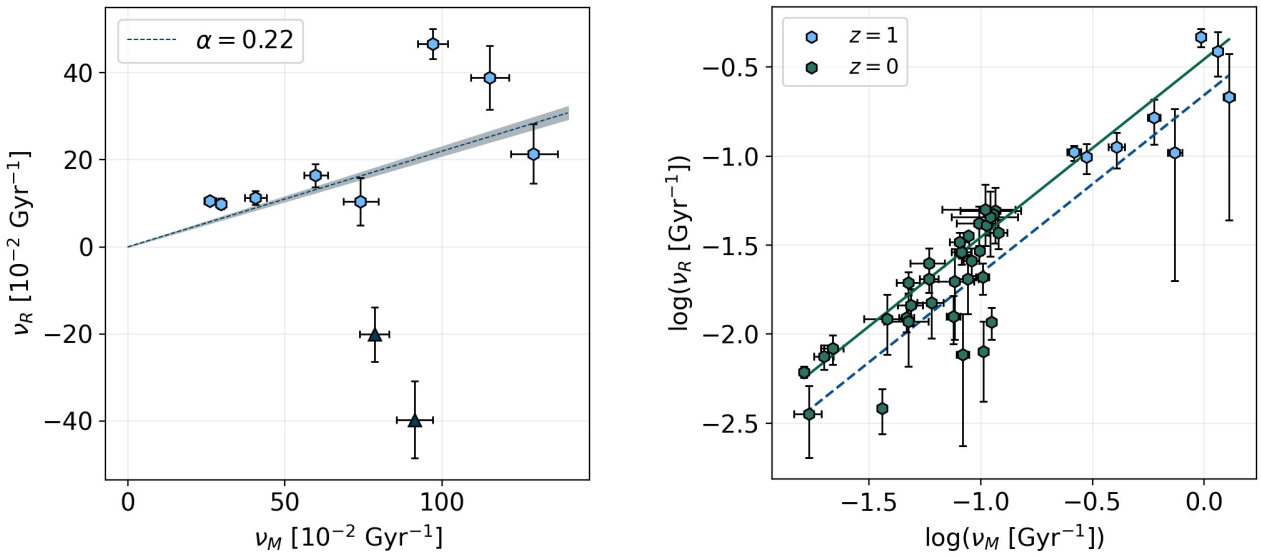

(a) **(b)**

Figure 4.4: a) Plot of specific radial growth rate versus specific mass growth rate of our sample. Galaxies with negative radial growth rate are indicated with the dark blue triangles. The dashed blue line is a line through the origin with slope $\alpha = 0.22$: the expected $\nu_R - \nu_M$ relation derived from the mass-size relation found by van der Wel et al. (2014). The shaded grey area indicates the uncertainty in α ($= \pm 0.01$). **b)** Same as Fig. 4.4a, but in double-logarithmic scale, therefore excluding galaxies with negative radial growth rate. Included are the growth rates found by P15, marked dark green. The solid green line is a line of slope 1, and intercept $\log \alpha = \log 0.35$.

4.3 Comparison with theoretical expectations

In Fig. 4.4a, we plot the radial growth rates versus mass growth rates of our sample. Following the discussion in Sec. 1.2.2, one of the empirical relations galaxies obey is the mass-size relation. In van der Wel et al. (2014), the mass-size relation for early- and late-types is determined over the redshift range $0 < z < 3$. For late-types, they find $R_s \propto M_*^{\alpha}$ with $\alpha = 0.22 \pm 0.01$ to hold in the entire redshift range (they find that the normalization, however, changes with redshift). In two steps, we show how this translates into the specific growth rates:

$$R_s = A M_*^{\alpha} \tag{4.5}$$

$$\ln R_s = \ln A + \alpha \ln M_* \tag{4.6}$$

$$\nu_R = \alpha \nu_M. \tag{4.7}$$

The last step involves taking the time-derivative on both sides, and for simplicity we assume that both the normalization A and coefficient α are time-independent (no evolution of the mass-size relation). As mentioned in Sec. 1.2.2, there is no consensus yet on the evolution of the mass-size relation, as some studies find that it evolves with redshift, while others find a universal relation. From Eq. 4.7, it follows that the growth rates should fall on a line through the origin with slope α (blue dashed line with shaded area indicating uncertainty in α). The outside-in growing galaxies are excluded from this statement. From the plot in Fig. 4.2 it is clear that the results generally agree with the expectations for a non-evolving mass-size relation, in particular the galaxies with $\nu_R < 30 \times 10^{-2}\,\mathrm{Gyr}^{-1}$. There is one obvious outlier with a radial growth rate exceeding $40 \times 10^{-2}\,\mathrm{Gyr}^{-1}$ at a mass growth rate just below $100 \times 10^{-2}\,\mathrm{Gyr}^{-1}$. However, outliers are expected, and the limited sample size prevents statistically strong conclusions.

In Fig. 4.4b, we plot the growth rates again. However this time the plot is double-logarithmic

and the $z \simeq 0$ galaxies from P15 are also included. This plot clearly demonstrates that galaxies at $z \simeq 1$ grow faster than galaxies at $z \simeq 0$, both in mass and radius. In logarithmic units, the relation in Eq. 4.7 becomes:

$$\log \nu_R = \log \alpha + \log \nu_M, \tag{4.8}$$

such that the points in this plot should fall on a line with intercept $\log \alpha$. The solid green line (with a slope of 1) has the adopted intercept $\alpha = 0.35$ by P15, calculated by combining the Tully-Fisher and Fall relation. The dashed blue line uses $\alpha = 0.22$ as empirically derived by van der Wel et al. (2014). Although it is difficult to see from the plot which value of α best represents the total distribution of points, it is interesting that points at $z \simeq 0$ and $z \simeq 1$ appear to align well on a straight line, as expected by the simple model indicated above. Note that an evolution of the mass-size relation (as found by some studies, see Sec. 1.2.2) would introduce an additional term in Eq. 4.7:

$$\nu_A = \frac{\mathrm{d}}{\mathrm{d}t}(\ln A(t)), \tag{4.9}$$

which would make the relation curve up or down. P15 found $|\nu_A| < 0.01\,\mathrm{Gyr}^{-1}$ for their sample. A similar estimate for our $z \simeq 1$ sample would be interesting to investigate, but is left for future work.

4.4 Discussion of uncertainties

Finally, we briefly discuss some possible limitations and sources of uncertainties of this work. First we discuss the impact that our choice of the S/N threshold has on our final results. Changing the threshold to 1.0 or 2.0 has a small impact on the inferred growth rates, but the resulting values are all within the current uncertainty ranges. Our results are thus largely independent of the choice for the S/N threshold. In Appendix A, we show a table of the total uncertainties.

One possible source of uncertainty is the choice of the return fraction $\mathscr{R}$. As mentioned in Sec. 1.3.3, the adopted value for $\mathscr{R} = 0.3$ is an intermediate value between choices of the IMF. Its value is uncertain in any case, since it is dependent on the choice of the IMF and the final-to-initial mass relation (P15). A higher or lower choice for this value would only increase or decrease the normalization of the SFRD model and thereby increase or decrease inferred growth rates by a fixed factor. The same holds for the uncertainty in stellar mass. Furthermore, since both growth rates are affected by the change in normalization equally, this implies that the dimensionless ratio between the two remains unchanged.

Perhaps the main limitation of this work is that we could not correct our measured Hα emission for dust extinction. To improve on this, it would be useful to obtain data in a larger wavelength range, including also Hβ, allowing a measurement of the Balmer decrement and therefore to correct for the effect of dust.

Chapter 5

Conclusions

5.1 Summary and conclusions

In this work we adopted a sample of 12 galaxies from the KROSS survey (Stott et al., 2016) at $z \simeq 1$ in order to investigate the inside-out growth scenario. We developed a fitting routine to fit 2D SFRD maps with the functions introduced in P15. Our routine was tested by fitting exponential profiles on a sample of three galaxies from the KMOS^{3D} survey (Wisnioski et al., 2019) to infer scale lengths. Results were compared with findings by W20 and agreed with them within the uncertainty ranges. This allowed us to conclude that our fitting routine is robust. We extracted Hα maps from the KMOS data cubes which were used as probes for the star formation rate distribution in our galaxies. Two galaxies were excluded from the final analysis due to a misaligned center. We inferred specific mass and radial growth rates, ν_M and ν_R, respectively, of the final sample, by using the SFRD fitting function from P15. Our specific mass growth rates are in agreement with findings for the star formation main sequence relation at $z \simeq 1$ in the respective mass range (Elbaz et al., 2007). 8/10 galaxies in our sample show significantly positive radial growth rates, and only two show negative radial growth rates.

5.1.1 Conclusions

We briefly summarize our conclusions:

1. Since 80% of our sample shows significant radial growth, we conclude that our results are consistent with the general picture of inside-out growth occurring at $z \simeq 1$.
2. We find that galaxies at $z \simeq 1$ grow ~ 7.5 times faster in mass and ~ 7 times faster in radius than their Local Universe counterparts. These results are in agreement with previous findings based on the main sequence of star formation.
3. Our results seem to be consistent with a model in which the mass-size relation is not strongly evolving with time, at least between $z \simeq 1$ and $z \simeq 0$.

5.2 Future work and improvements

One substantial caveat in this work is the fact that our SFRD profiles are not corrected for dust. Future research could improve findings by including a dust correction from the Balmer decrement. Furthermore, our results are complicated by the low spatial resolution of the Hα maps. With the advent of new telescopes and equipment, such as the Extremely Large Telescope (ELT) with its Extremely Adaptive Optics system, spatially resolved spectroscopy be made possible at a significantly higher spatial resolution. The specific radial growth rate is a remarkable measure

for inside-out growth of galaxies. Probing even higher redshifts with this technique could consolidate evidence for the inside-out growth scenario. Finally, the relation of ν_R and ν_M provides a powerful tool to inspect the evolution of the mass-size relation.

Chapter 6

Acknowledgements

First off I would like to greatly thank prof. dr. Filippo Fraternali for allowing me to work on this project, and supervising me over the course of a year. This thesis was written during the COVID-19 pandemic, which meant that 'real' meetings, with a blackboard full of equations and drawings, one or more cups of coffee, and the additional small-talk before and/or after, were impossible for the majority of the project. This period was not always easy for me, but Filippo showed real understanding, offered support where he could and provided excellent feedback. I want to thank my second supervisor, dr. Gabriele Pezzulli, for his incredible devotion to explain all the fine details of the treated theory, his immediate replies to questions, thorough feedback, and overall great involvement in the project. I also want to express my gratitude towards Casper Farret Jentink, not only for being a friend, but also for providing me with lots of insights and useful discussions. Dr. Antonino Marasco deserves to be mentioned as he supplied the basis for the code developed in this thesis and offered to help me with any questions, which I sincerely appreciated. Furthermore, I thank dr. Enrico Di Teodoro for his help with the software BBAROLO. Finally, I want to thank my friends Bart van Rijswijk, Colin Broer, Nikki Potze, Maik van Rijn, Mart Roozeboom, Mathijn Lensen and Tijmen Jansen for their support.

Bibliography

M. Aumer and S. D. M. White. Idealized models for galactic disc formation and evolution in 'realistic' ΛCDM haloes. , 428(2):1055–1076, Jan. 2013. doi: 10.1093/mnras/sts083.

M. Aumer, S. D. M. White, and T. Naab. The diverse formation histories of simulated disc galaxies. , 441(4):3679–3695, July 2014. doi: 10.1093/mnras/stu818.

P. S. Behroozi and J. Silk. A Simple Technique for Predicting High-redshift Galaxy Evolution. , 799(1):32, Jan. 2015. doi: 10.1088/0004-637X/799/1/32.

G. B. Brammer, P. G. van Dokkum, M. Franx, M. Fumagalli, S. Patel, H.-W. Rix, R. E. Skelton, M. Kriek, E. Nelson, K. B. Schmidt, R. Bezanson, E. da Cunha, D. K. Erb, X. Fan, N. Förster Schreiber, G. D. Illingworth, I. Labbé, J. Leja, B. Lundgren, D. Magee, D. Marchesini, P. McCarthy, I. Momcheva, A. Muzzin, R. Quadri, C. C. Steidel, T. Tal, D. Wake, K. E. Whitaker, and A. Williams. 3D-HST: A Wide-field Grism Spectroscopic Survey with the Hubble Space Telescope. , 200(2):13, June 2012. doi: 10.1088/0067-0049/200/2/13.

J. S. Bullock and M. Boylan-Kolchin. Small-Scale Challenges to the ΛCDM Paradigm. , 55(1): 343–387, Aug. 2017. doi: 10.1146/annurev-astro-091916-055313.

J. S. Bullock, A. Dekel, T. S. Kolatt, A. V. Kravtsov, A. A. Klypin, C. Porciani, and J. R. Primack. A Universal Angular Momentum Profile for Galactic Halos. , 555(1):240–257, July 2001. doi: 10.1086/321477.

D. Calzetti, R. C. Kennicutt, C. W. Engelbracht, C. Leitherer, B. T. Draine, L. Kewley, J. Moustakas, M. Sosey, D. A. Dale, K. D. Gordon, G. X. Helou, D. J. Hollenbach, L. Armus, G. Bendo, C. Bot, B. Buckalew, T. Jarrett, A. Li, M. Meyer, E. J. Murphy, M. Prescott, M. W. Regan, G. H. Rieke, H. Roussel, K. Sheth, J. D. T. Smith, M. D. Thornley, and F. Walter. The Calibration of Mid-Infrared Star Formation Rate Indicators. , 666(2):870–895, Sept. 2007. doi: 10.1086/520082.

A. Cimatti, F. Fraternali, and C. Nipoti. *Introduction to Galaxy Formation and Evolution: From Primordial Gas to Present-Day Galaxies*. 2019.

L. Ciotti. Stellar systems following the R1/m luminosity law. , 249:99–106, Sept. 1991.

M. C. Cooper, J. A. Newman, D. J. Croton, B. J. Weiner, C. N. A. Willmer, B. F. Gerke, D. S. Madgwick, S. M. Faber, M. Davis, A. L. Coil, D. P. Finkbeiner, P. Guhathakurta, and D. C. Koo. The DEEP2 Galaxy Redshift Survey: the relationship between galaxy properties and environment at z $\sim$1. , 370(1):198–212, July 2006. doi: 10.1111/j.1365-2966.2006.10485.x.

L. L. Cowie, A. Songaila, E. M. Hu, and J. G. Cohen. New Insight on Galaxy Formation and Evolution From Keck Spectroscopy of the Hawaii Deep Fields. , 112:839, Sept. 1996. doi: 10.1086/118058.

E. Curtis-Lake, R. J. McLure, J. S. Dunlop, M. Schenker, A. B. Rogers, T. Targett, M. Cirasuolo, O. Almaini, M. L. N. Ashby, E. J. Bradshaw, S. L. Finkelstein, M. Dickinson, R. S. Ellis, S. M. Faber, G. G. Fazio, H. C. Ferguson, A. Fontana, N. A. Grogin, W. G. Hartley, D. D. Kocevski, A. M.

Koekemoer, K. Lai, B. E. Robertson, E. Vanzella, and S. P. Willner. The ages, masses and star formation rates of spectroscopically confirmed z $\sim$ 6 galaxies in CANDELS. , 429(1):302–322, Feb. 2013. doi: 10.1093/mnras/sts338.

R. I. Davies, A. Agudo Berbel, E. Wiezorrek, M. Cirasuolo, N. M. Förster Schreiber, Y. Jung, B. Muschielok, T. Ott, S. Ramsay, J. Schlichter, R. Sharples, and M. Wegner. The Software Package for Astronomical Reductions with KMOS: SPARK. , 558:A56, Oct. 2013. doi: 10.1051/0004-6361/201322282.

G. de Vaucouleurs. Recherches sur les Nebuleuses Extragalactiques. *Annales d'Astrophysique*, 11: 247, Jan. 1948.

A. Dekel and J. Ostriker. *Formation of Structure in the Universe*. Apr. 1999.

E. M. Di Teodoro and F. Fraternali. ^{3D} BAROLO: a new 3D algorithm to derive rotation curves of galaxies. , 451(3):3021–3033, Aug. 2015. doi: 10.1093/mnras/stv1213.

E. M. Di Teodoro, F. Fraternali, and S. H. Miller. Flat rotation curves and low velocity dispersions in KMOS star-forming galaxies at z $\sim$1. , 594:A77, Oct. 2016. doi: 10.1051/0004-6361/201628315.

P. Dimauro, M. Huertas-Company, E. Daddi, P. G. Pérez-González, M. Bernardi, F. Caro, A. Cattaneo, B. Häußler, U. Kuchner, F. Shankar, G. Barro, F. Buitrago, S. M. Faber, D. D. Kocevski, A. M. Koekemoer, D. C. Koo, S. Mei, R. Peletier, J. Primack, A. Rodriguez-Puebla, M. Salvato, and D. Tuccillo. The structural properties of classical bulges and discs from z $\sim$ 2. , 489(3): 4135–4154, Nov. 2019. doi: 10.1093/mnras/stz2421.

A. Domínguez, B. Siana, A. L. Henry, C. Scarlata, A. G. Bedregal, M. Malkan, H. Atek, N. R. Ross, J. W. Colbert, H. I. Teplitz, M. Rafelski, P. McCarthy, A. Bunker, N. P. Hathi, A. Dressler, C. L. Martin, and D. Masters. Dust Extinction from Balmer Decrements of Star-forming Galaxies at 0.75 <= z <= 1.5 with Hubble Space Telescope/Wide-Field-Camera 3 Spectroscopy from the WFC3 Infrared Spectroscopic Parallel Survey. , 763(2):145, Feb. 2013. doi: 10.1088/0004-637X/763/2/145.

A. A. Dutton and F. C. van den Bosch. The angular momentum of disc galaxies: implications for gas accretion, outflows, and dynamical friction. , 421(1):608–620, Mar. 2012. doi: 10.1111/j.1365-2966.2011.20339.x.

O. J. Eggen, D. Lynden-Bell, and A. R. Sandage. Evidence from the motions of old stars that the Galaxy collapsed. , 136:748, Nov. 1962. doi: 10.1086/147433.

D. Elbaz, E. Daddi, D. Le Borgne, M. Dickinson, D. M. Alexander, R. R. Chary, J. L. Starck, W. N. Brandt, M. Kitzbichler, E. MacDonald, M. Nonino, P. Popesso, D. Stern, and E. Vanzella. The reversal of the star formation-density relation in the distant universe. , 468(1):33–48, June 2007. doi: 10.1051/0004-6361:20077525.

D. Elbaz, M. Dickinson, H. S. Hwang, T. Díaz-Santos, G. Magdis, B. Magnelli, D. Le Borgne, F. Galliano, M. Pannella, P. Chanial, L. Armus, V. Charmandaris, E. Daddi, H. Aussel, P. Popesso, J. Kartaltepe, B. Altieri, I. Valtchanov, D. Coia, H. Dannerbauer, K. Dasyra, R. Leiton, J. Mazzarella, D. M. Alexander, V. Buat, D. Burgarella, R. R. Chary, R. Gilli, R. J. Ivison, S. Juneau, E. Le Floc'h, D. Lutz, G. E. Morrison, J. R. Mullaney, E. Murphy, A. Pope, D. Scott, M. Brodwin, D. Calzetti, C. Cesarsky, S. Charlot, H. Dole, P. Eisenhardt, H. C. Ferguson, N. Förster Schreiber, D. Frayer, M. Giavalisco, M. Huynh, A. M. Koekemoer, C. Papovich, N. Reddy, C. Surace, H. Teplitz, M. S. Yun, and G. Wilson. GOODS-Herschel: an infrared main sequence for star-forming galaxies. , 533:A119, Sept. 2011. doi: 10.1051/0004-6361/201117239.

ESO. KMOS Instrument Description, 2013. URL https://www.eso.org/sci/facilities/paranal/instruments/kmos/inst.html.

S. M. Fall. Galaxy formation - Some comparisons between theory and observation. In E. Athanassoula, editor, *Internal Kinematics and Dynamics of Galaxies*, volume 100, pages 391–398, Jan. 1983.

S. M. Fall and G. Efstathiou. Formation and rotation of disc galaxies with haloes. , 193:189–206, Oct. 1980. doi: 10.1093/mnras/193.2.189.

K. Fathi, M. Gatchell, E. Hatziminaoglou, and B. Epinat. Disc scalelengths out to redshift 5.8. , 423(1):L112–L116, June 2012. doi: 10.1111/j.1745-3933.2012.01270.x.

F. Fraternali and M. Tomassetti. Estimating gas accretion in disc galaxies using the Kennicutt-Schmidt law. , 426(3):2166–2177, Nov. 2012. doi: 10.1111/j.1365-2966.2012.21650.x.

D. Goddard, D. Thomas, C. Maraston, K. Westfall, J. Etherington, R. Riffel, N. D. Mallmann, Z. Zheng, M. Argudo-Fernández, J. Lian, M. Bershady, K. Bundy, N. Drory, D. Law, R. Yan, D. Wake, A. Weijmans, D. Bizyaev, J. Brownstein, R. R. Lane, R. Maiolino, K. Masters, M. Merrifield, C. Nitschelm, K. Pan, A. Roman-Lopes, T. Storchi-Bergmann, and D. P. Schneider. SDSS-IV MaNGA: Spatially resolved star formation histories in galaxies as a function of galaxy mass and type. , 466(4):4731–4758, Apr. 2017. doi: 10.1093/mnras/stw3371.

S. M. Gogarten, J. J. Dalcanton, B. F. Williams, R. Roškar, J. Holtzman, A. C. Seth, A. Dolphin, D. Weisz, A. Cole, V. P. Debattista, K. M. Gilbert, K. Olsen, E. Skillman, R. S. de Jong, I. D. Karachentsev, and T. R. Quinn. The Advanced Camera for Surveys Nearby Galaxy Survey Treasury. V. Radial Star Formation History of NGC 300. , 712(2):858–874, Apr. 2010. doi: 10.1088/0004-637X/712/2/858.

R. M. González Delgado, R. García-Benito, E. Pérez, R. Cid Fernandes, A. L. de Amorim, C. Cortijo-Ferrero, E. A. D. Lacerda, R. López Fernández, N. Vale-Asari, S. F. Sánchez, M. Mollá, T. Ruiz-Lara, P. Sánchez-Blázquez, C. J. Walcher, J. Alves, J. A. L. Aguerri, S. Bekeraité, J. Bland-Hawthorn, L. Galbany, A. Gallazzi, B. Husemann, J. Iglesias-Páramo, V. Kalinova, A. R. López-Sánchez, R. A. Marino, I. Márquez, J. Masegosa, D. Mast, J. Méndez-Abreu, A. Mendoza, A. del Olmo, I. Pérez, A. Quirrenbach, and S. Zibetti. The CALIFA survey across the Hubble sequence. Spatially resolved stellar population properties in galaxies. , 581:A103, Sept. 2015. doi: 10.1051/0004-6361/201525938.

N. A. Grogin, D. D. Kocevski, S. M. Faber, H. C. Ferguson, A. M. Koekemoer, A. G. Riess, V. Acquaviva, D. M. Alexander, O. Almaini, M. L. N. Ashby, M. Barden, E. F. Bell, F. Bournaud, T. M. Brown, K. I. Caputi, S. Casertano, P. Cassata, M. Castellano, P. Challis, R.-R. Chary, E. Cheung, M. Cirasuolo, C. J. Conselice, A. Roshan Cooray, D. J. Croton, E. Daddi, T. Dahlen, R. Davé, D. F. de Mello, A. Dekel, M. Dickinson, T. Dolch, J. L. Donley, J. S. Dunlop, A. A. Dutton, D. Elbaz, G. G. Fazio, A. V. Filippenko, S. L. Finkelstein, A. Fontana, J. P. Gardner, P. M. Garnavich, E. Gawiser, M. Giavalisco, A. Grazian, Y. Guo, N. P. Hathi, B. Häussler, P. F. Hopkins, J.-S. Huang, K.-H. Huang, S. W. Jha, J. S. Kartaltepe, R. P. Kirshner, D. C. Koo, K. Lai, K.-S. Lee, W. Li, J. M. Lotz, R. A. Lucas, P. Madau, P. J. McCarthy, E. J. McGrath, D. H. McIntosh, R. J. McLure, B. Mobasher, L. A. Moustakas, M. Mozena, K. Nandra, J. A. Newman, S.-M. Niemi, K. G. Noeske, C. J. Papovich, L. Pentericci, A. Pope, J. R. Primack, A. Rajan, S. Ravindranath, N. A. Reddy, A. Renzini, H.-W. Rix, A. R. Robaina, S. A. Rodney, D. J. Rosario, P. Rosati, S. Salimbeni, C. Scarlata, B. Siana, L. Simard, J. Smidt, R. S. Somerville, H. Spinrad, A. N. Straughn, L.-G. Strolger, O. Telford, H. I. Teplitz, J. R. Trump, A. van der Wel, C. Villforth, R. H. Wechsler, B. J. Weiner, T. Wiklind, V. Wild, G. Wilson, S. Wuyts, H.-J. Yan, and M. S. Yun. CANDELS: The Cosmic Assembly Near-infrared Deep Extragalactic Legacy Survey. , 197(2):35, Dec. 2011. doi: 10.1088/0067-0049/197/2/35.

Q. Guo, S. White, C. Li, and M. Boylan-Kolchin. How do galaxies populate dark matter haloes? , 404(3):1111–1120, May 2010. doi: 10.1111/j.1365-2966.2010.16341.x.

C. M. Harrison, H. L. Johnson, A. M. Swinbank, J. P. Stott, R. G. Bower, I. Smail, A. L. Tiley, A. J. Bunker, M. Cirasuolo, D. Sobral, R. M. Sharples, P. Best, M. Bureau, M. J. Jarvis, and G. Magdis. The KMOS Redshift One Spectroscopic Survey (KROSS): rotational velocities and angular momentum of z ≈ 0.9 galaxies. , 467(2):1965–1983, May 2017. doi: 10.1093/mnras/stx217.

B. P. Holden, M. Franx, G. D. Illingworth, M. Postman, A. van der Wel, D. D. Kelson, J. P. Blakeslee, H. Ford, R. Demarco, and S. Mei. The Ellipticities of Cluster Early-type Galaxies from z ∼1 to z ∼0: No Evolution in the Overall Distribution of Bulge-to-Disk Ratios. , 693(1):617–633, Mar. 2009. doi: 10.1088/0004-637X/693/1/617.

T. Ichikawa, M. Kajisawa, and M. Akhlaghi. A universal stellar mass-size relation of galaxies in the GOODS-North region. , 422(2):1014–1027, May 2012. doi: 10.1111/j.1365-2966.2012.20674.x.

A. Jenkins, C. S. Frenk, S. D. M. White, J. M. Colberg, S. Cole, A. E. Evrard, H. M. P. Couchman, and N. Yoshida. The mass function of dark matter haloes. , 321(2):372–384, Feb. 2001. doi: 10.1046/j.1365-8711.2001.04029.x.

W. A. Joye and E. Mandel. New Features of SAOImage DS9. In H. E. Payne, R. I. Jedrzejewski, and R. N. Hook, editors, *Astronomical Data Analysis Software and Systems XII*, volume 295 of *Astronomical Society of the Pacific Conference Series*, page 489, Jan. 2003.

R. Kennedy, S. P. Bamford, B. Häußler, S. Brough, B. Holwerda, A. M. Hopkins, M. Vika, and B. Vulcani. Galaxy And Mass Assembly (GAMA): Galaxy colour gradients versus colour, structure, and luminosity. , 593:A84, Sept. 2016. doi: 10.1051/0004-6361/201628715.

J. Kennicutt, Robert C. Star Formation in Galaxies Along the Hubble Sequence. , 36:189–232, Jan. 1998. doi: 10.1146/annurev.astro.36.1.189.

R. C. Kennicutt and N. J. Evans. Star Formation in the Milky Way and Nearby Galaxies. , 50:531–608, Sept. 2012. doi: 10.1146/annurev-astro-081811-125610.

A. A. Klypin, S. Trujillo-Gomez, and J. Primack. Dark Matter Halos in the Standard Cosmological Model: Results from the Bolshoi Simulation. , 740(2):102, Oct. 2011. doi: 10.1088/0004-637X/740/2/102.

A. M. Koekemoer, S. M. Faber, H. C. Ferguson, N. A. Grogin, D. D. Kocevski, D. C. Koo, K. Lai, J. M. Lotz, R. A. Lucas, E. J. McGrath, S. Ogaz, A. Rajan, A. G. Riess, S. A. Rodney, L. Strolger, S. Casertano, M. Castellano, T. Dahlen, M. Dickinson, T. Dolch, A. Fontana, M. Giavalisco, A. Grazian, Y. Guo, N. P. Hathi, K.-H. Huang, A. van der Wel, H.-J. Yan, V. Acquaviva, D. M. Alexander, O. Almaini, M. L. N. Ashby, M. Barden, E. F. Bell, F. Bournaud, T. M. Brown, K. I. Caputi, P. Cassata, P. J. Challis, R.-R. Chary, E. Cheung, M. Cirasuolo, C. J. Conselice, A. Roshan Cooray, D. J. Croton, E. Daddi, R. Davé, D. F. de Mello, L. de Ravel, A. Dekel, J. L. Donley, J. S. Dunlop, A. A. Dutton, D. Elbaz, G. G. Fazio, A. V. Filippenko, S. L. Finkelstein, C. Frazer, J. P. Gardner, P. M. Garnavich, E. Gawiser, R. Gruetzbauch, W. G. Hartley, B. Häussler, J. Herrington, P. F. Hopkins, J.-S. Huang, S. W. Jha, A. Johnson, J. S. Kartaltepe, A. A. Khostovan, R. P. Kirshner, C. Lani, K.-S. Lee, W. Li, P. Madau, P. J. McCarthy, D. H. McIntosh, R. J. McLure, C. McPartland, B. Mobasher, H. Moreira, A. Mortlock, L. A. Moustakas, M. Mozena, K. Nandra, J. A. Newman, J. L. Nielsen, S. Niemi, K. G. Noeske, C. J. Papovich, L. Pentericci, A. Pope, J. R. Primack, S. Ravindranath, N. A. Reddy, A. Renzini, H.-W. Rix, A. R. Robaina, D. J. Rosario, P. Rosati,

S. Salimbeni, C. Scarlata, B. Siana, L. Simard, J. Smidt, D. Snyder, R. S. Somerville, H. Spinrad, A. N. Straughn, O. Telford, H. I. Teplitz, J. R. Trump, C. Vargas, C. Villforth, C. R. Wagner, P. Wandro, R. H. Wechsler, B. J. Weiner, T. Wiklind, V. Wild, G. Wilson, S. Wuyts, and M. S. Yun. CANDELS: The Cosmic Assembly Near-infrared Deep Extragalactic Legacy Survey—The Hubble Space Telescope Observations, Imaging Data Products, and Mosaics. , 197(2):36, Dec. 2011. doi: 10.1088/0067-0049/197/2/36.

P. Kroupa and C. Weidner. Galactic-Field Initial Mass Functions of Massive Stars. , 598(2):1076–1078, Dec. 2003. doi: 10.1086/379105.

C. d. P. Lagos. Angular momentum evolution of galaxies: the perspective of hydrodynamical simulations. *arXiv e-prints*, art. arXiv:1810.13074, Oct. 2018.

C. Li, E. Wang, L. Lin, M. A. Bershady, K. Bundy, C. A. Tremonti, T. Xiao, R. Yan, D. Bizyaev, M. Blanton, S. Cales, B. Cherinka, E. Cheung, N. Drory, E. Emsellem, H. Fu, J. Gelfand, D. R. Law, L. Lin, N. MacDonald, C. Maraston, K. L. Masters, M. R. Merrifield, K. Pan, S. F. Sánchez, D. P. Schneider, D. Thomas, D. Wake, L. Wang, A.-M. Weijmans, D. Wilkinson, P. Yoachim, K. Zhang, and T. Zheng. P-MaNGA: Gradients in Recent Star Formation Histories as Diagnostics for Galaxy Growth and Death. , 804(2):125, May 2015. doi: 10.1088/0004-637X/804/2/125.

A. Marasco, F. Fraternali, L. Posti, M. Ijtsma, E. M. Di Teodoro, and T. Oosterloo. The angular momentum of disc galaxies at z = 1. , 621:L6, Jan. 2019. doi: 10.1051/0004-6361/201834456.

F. Marinacci, F. Fraternali, J. Binney, C. Nipoti, L. Ciotti, and P. Londrillo. Fountain-driven gas accretion by the Milky Way. In *European Physical Journal Web of Conferences*, volume 19 of *European Physical Journal Web of Conferences*, page 08008, Feb. 2012. doi: 10.1051/epjconf/20121908008.

E. Mieda, S. A. Wright, J. E. Larkin, L. Armus, S. Juneau, S. Salim, and N. Murray. IROCKS: Spatially Resolved Kinematics of z $\sim$ 1 Star-forming Galaxies. , 831(1):78, Nov. 2016. doi: 10.3847/0004-637X/831/1/78.

H. J. Mo, S. Mao, and S. D. M. White. The formation of galactic discs. , 295(2):319–336, Apr. 1998. doi: 10.1046/j.1365-8711.1998.01227.x.

A. F. J. Moffat. A Theoretical Investigation of Focal Stellar Images in the Photographic Emulsion and Application to Photographic Photometry. , 3:455, Dec. 1969.

M. Mollá and A. I. Díaz. A grid of chemical evolution models as a tool to interpret spiral and irregular galaxies data. , 358(2):521–543, Apr. 2005. doi: 10.1111/j.1365-2966.2005.08782.x.

M. Mosleh, S. Hosseinnejad, S. Z. Hosseini-ShahiSavandi, and S. Tacchella. Galaxy Sizes Since z = 2 from the Perspective of Stellar Mass Distribution within Galaxies. , 905(2):170, Dec. 2020. doi: 10.3847/1538-4357/abc7cc.

L. A. Mowla, P. van Dokkum, G. B. Brammer, I. Momcheva, A. van der Wel, K. Whitaker, E. Nelson, R. Bezanson, A. Muzzin, M. Franx, J. MacKenty, J. Leja, M. Kriek, and D. Marchesini. COSMOS-DASH: The Evolution of the Galaxy Size-Mass Relation since z $\sim$ 3 from New Wide-field WFC3 Imaging Combined with CANDELS/3D-HST. , 880(1):57, July 2019. doi: 10.3847/1538-4357/ab290a.

J. C. Muñoz-Mateos, A. Gil de Paz, S. Boissier, J. Zamorano, T. Jarrett, J. Gallego, and B. F. Madore. Specific Star Formation Rate Profiles in Nearby Spiral Galaxies: Quantifying the Inside-Out Formation of Disks. , 658(2):1006–1026, Apr. 2007. doi: 10.1086/511812.

J. C. Muñoz-Mateos, A. Gil de Paz, S. Boissier, J. Zamorano, D. A. Dale, P. G. Pérez-González, J. Gallego, B. F. Madore, G. Bendo, M. D. Thornley, B. T. Draine, A. Boselli, V. Buat, D. Calzetti, J. Moustakas, and J. Kennicutt, R. C. Radial Distribution of Stars, Gas, and Dust in Sings Galaxies. II. Derived Dust Properties. , 701(2):1965–1991, Aug. 2009a. doi: 10.1088/0004-637X/701/2/1965.

J. C. Muñoz-Mateos, A. Gil de Paz, J. Zamorano, S. Boissier, D. A. Dale, P. G. Pérez-González, J. Gallego, B. F. Madore, G. Bendo, A. Boselli, V. Buat, D. Calzetti, J. Moustakas, and J. Kennicutt, R. C. Radial Distribution of Stars, Gas, and Dust in SINGS Galaxies. I. Surface Photometry and Morphology. , 703(2):1569–1596, Oct. 2009b. doi: 10.1088/0004-637X/703/2/1569.

J. F. Navarro and M. Steinmetz. The Effects of a Photoionizing Ultraviolet Background on the Formation of Disk Galaxies. , 478(1):13–28, Mar. 1997. doi: 10.1086/303763.

K. V. Nedkova, B. Häußler, D. Marchesini, P. Dimauro, G. Brammer, P. Eigenthaler, A. D. Feinstein, H. C. Ferguson, M. Huertas-Company, E. J. Johnston, E. Kado-Fong, J. S. Kartaltepe, I. Labbé, D. Lange-Vagle, N. S. Martis, E. J. McGrath, A. Muzzin, P. Oesch, Y. Ordenes-Briceño, T. Puzia, H. V. Shipley, B. D. Simmons, R. E. Skelton, M. Stefanon, A. van der Wel, and K. E. Whitaker. Extending the evolution of the stellar mass - size relation at $z \leq 2$ to low stellar mass galaxies from HFF and CANDELS. , June 2021. doi: 10.1093/mnras/stab1744.

E. J. Nelson, P. G. van Dokkum, G. Brammer, N. Förster Schreiber, M. Franx, M. Fumagalli, S. Patel, H.-W. Rix, R. E. Skelton, R. Bezanson, E. Da Cunha, M. Kriek, I. Labbe, B. Lundgren, R. Quadri, and K. B. Schmidt. Spatially Resolved Hα Maps and Sizes of 57 Strongly Star-forming Galaxies at $z \sim 1$ from 3D-HST: Evidence for Rapid Inside-out Assembly of Disk Galaxies. , 747(2):L28, Mar. 2012. doi: 10.1088/2041-8205/747/2/L28.

M. Newville, T. Stensitzki, D. B. Allen, and A. Ingargiola. LMFIT: Non-Linear Least-Square Minimization and Curve-Fitting for Python, Sept. 2014. URL https://doi.org/10.5281/zenodo.11813.

P. J. E. Peebles. Origin of the Angular Momentum of Galaxies. , 155:393, Feb. 1969. doi: 10.1086/149876.

G. Pezzulli, F. Fraternali, S. Boissier, and J. C. Muñoz-Mateos. The instantaneous radial growth rate of stellar discs. , 451(3):2324–2336, Aug. 2015. doi: 10.1093/mnras/stv1077.

G. Pezzulli, F. Fraternali, and J. Binney. The angular momentum of cosmological coronae and the inside-out growth of spiral galaxies. , 467(1):311–329, May 2017. doi: 10.1093/mnras/stx029.

A. Pillepich, V. Springel, D. Nelson, S. Genel, J. Naiman, R. Pakmor, L. Hernquist, P. Torrey, M. Vogelsberger, R. Weinberger, and F. Marinacci. Simulating galaxy formation with the IllustrisTNG model. , 473(3):4077–4106, Jan. 2018. doi: 10.1093/mnras/stx2656.

L. Piovan, R. Tantalo, and C. Chiosi. Modelling galaxy spectra in presence of interstellar dust - II. From the ultraviolet to the far-infrared. , 370(3):1454–1478, Aug. 2006. doi: 10.1111/j.1365-2966.2006.10573.x.

E. Ricciardelli and A. Franceschini. GECO: Galaxy Evolution COde - A new semi-analytical model of galaxy formation. , 518:A14, July 2010. doi: 10.1051/0004-6361/200913374.

G. H. Rieke, A. Alonso-Herrero, B. J. Weiner, P. G. Pérez-González, M. Blaylock, J. L. Donley, and D. Marcillac. Determining Star Formation Rates for Infrared Galaxies. , 692(1):556–573, Feb. 2009. doi: 10.1088/0004-637X/692/1/556.

R. Roškar, V. P. Debattista, T. R. Quinn, and J. Wadsley. Radial migration in disc galaxies - I. Transient spiral structure and dynamics. , 426(3):2089–2106, Nov. 2012. doi: 10.1111/j.1365-2966.2012.21860.x.

S. Salim, R. M. Rich, S. Charlot, J. Brinchmann, B. D. Johnson, D. Schiminovich, M. Seibert, R. Mallery, T. M. Heckman, K. Forster, P. G. Friedman, D. C. Martin, P. Morrissey, S. G. Neff, T. Small, T. K. Wyder, L. Bianchi, J. Donas, Y.-W. Lee, B. F. Madore, B. Milliard, A. S. Szalay, B. Y. Welsh, and S. K. Yi. UV Star Formation Rates in the Local Universe. , 173(2):267–292, Dec. 2007. doi: 10.1086/519218.

P. Sánchez-Blázquez, F. F. Rosales-Ortega, J. Méndez-Abreu, I. Pérez, S. F. Sánchez, S. Zibetti, J. A. L. Aguerri, J. Bland-Hawthorn, C. Catalán-Torrecilla, R. Cid Fernandes, A. de Amorim, A. de Lorenzo-Caceres, J. Falcón-Barroso, A. Galazzi, R. García Benito, A. Gil de Paz, R. González Delgado, B. Husemann, J. Iglesias-Páramo, B. Jungwiert, R. A. Marino, I. Márquez, D. Mast, M. A. Mendoza, M. Mollá, P. Papaderos, T. Ruiz-Lara, G. van de Ven, C. J. Walcher, and L. Wisotzki. Stellar population gradients in galaxy discs from the CALIFA survey. The influence of bars. , 570:A6, Oct. 2014. doi: 10.1051/0004-6361/201423635.

P. Santini, H. C. Ferguson, A. Fontana, B. Mobasher, G. Barro, M. Castellano, S. L. Finkelstein, A. Grazian, L. T. Hsu, B. Lee, S. K. Lee, J. Pforr, M. Salvato, T. Wiklind, S. Wuyts, O. Almaini, M. C. Cooper, A. Galametz, B. Weiner, R. Amorin, K. Boutsia, C. J. Conselice, T. Dahlen, M. E. Dickinson, M. Giavalisco, N. A. Grogin, Y. Guo, N. P. Hathi, D. Kocevski, A. M. Koekemoer, P. Kurczynski, E. Merlin, A. Mortlock, J. A. Newman, D. Paris, L. Pentericci, R. Simons, and S. P. Willner. Stellar Masses from the CANDELS Survey: The GOODS-South and UDS Fields. , 801 (2):97, Mar. 2015. doi: 10.1088/0004-637X/801/2/97.

J. A. Sellwood and J. J. Binney. Radial mixing in galactic discs. , 336(3):785–796, Nov. 2002. doi: 10.1046/j.1365-8711.2002.05806.x.

J. L. Sérsic. Influence of the atmospheric and instrumental dispersion on the brightness distribution in a galaxy. *Boletin de la Asociacion Argentina de Astronomia La Plata Argentina*, 6:41–43, Feb. 1963.

R. Sharples, R. Bender, A. Agudo Berbel, N. Bezawada, R. Castillo, M. Cirasuolo, G. Davidson, R. Davies, M. Dubbeldam, A. Fairley, G. Finger, N. Förster Schreiber, F. Gonte, A. Hess, I. Jung, I. Lewis, J. L. Lizon, B. Muschielok, L. Pasquini, J. Pirard, D. Popovic, S. Ramsay, P. Rees, J. Richter, M. Riquelme, M. Rodrigues, I. Saviane, J. Schlichter, L. Schmidtobreick, A. Segovia, A. Smette, T. Szeifert, A. van Kesteren, M. Wegner, and E. Wiezorrek. First Light for the KMOS Multi-Object Integral-Field Spectrometer. *The Messenger*, 151:21–23, Mar. 2013.

R. E. Skelton, K. E. Whitaker, I. G. Momcheva, G. B. Brammer, P. G. van Dokkum, I. Labbé, M. Franx, A. van der Wel, R. Bezanson, E. Da Cunha, M. Fumagalli, N. Förster Schreiber, M. Kriek, J. Leja, B. F. Lundgren, D. Magee, D. Marchesini, M. V. Maseda, E. J. Nelson, P. Oesch, C. Pacifici, S. G. Patel, S. Price, H.-W. Rix, T. Tal, D. A. Wake, and S. Wuyts. 3D-HST WFC3-selected Photometric Catalogs in the Five CANDELS/3D-HST Fields: Photometry, Photometric Redshifts, and Stellar Masses. , 214(2):24, Oct. 2014. doi: 10.1088/0067-0049/214/2/24.

M. W. L. Smith, S. A. Eales, I. De Looze, M. Baes, G. J. Bendo, S. Bianchi, M. Boquien, A. Boselli, V. Buat, L. Ciesla, M. Clemens, D. L. Clements, A. R. Cooray, L. Cortese, J. I. Davies, J. Fritz, H. L. Gomez, T. M. Hughes, O. Ł. Karczewski, N. Lu, S. J. Oliver, A. Remy-Ruyer, L. Spinoglio, and S. Viaene. Far-reaching dust distribution in galaxy discs. , 462(1):331–344, Oct. 2016. doi: 10.1093/mnras/stw1611.

R. S. Somerville and R. Davé. Physical Models of Galaxy Formation in a Cosmological Framework. , 53:51–113, Aug. 2015. doi: 10.1146/annurev-astro-082812-140951.

J. S. Speagle, C. L. Steinhardt, P. L. Capak, and J. D. Silverman. A Highly Consistent Framework for the Evolution of the Star-Forming "Main Sequence" from z ∼0-6. , 214(2):15, Oct. 2014. doi: 10.1088/0067-0049/214/2/15.

J. P. Stott, A. M. Swinbank, H. L. Johnson, A. Tiley, G. Magdis, R. Bower, A. J. Bunker, M. Bureau, C. M. Harrison, M. J. Jarvis, R. Sharples, I. Smail, D. Sobral, P. Best, and M. Cirasuolo. The KMOS Redshift One Spectroscopic Survey (KROSS): dynamical properties, gas and dark matter fractions of typical z ∼ 1 star-forming galaxies. , 457(2):1888–1904, Apr. 2016. doi: 10.1093/mnras/stw129.

V. A. Taylor, R. A. Jansen, R. A. Windhorst, S. C. Odewahn, and J. E. Hibbard. UBVR and Hubble Space Telescope Mid-Ultraviolet and Near-Infrared Surface Photometry and Radial Color Gradients of Late-Type, Irregular, and Peculiar Galaxies. , 630(2):784–803, Sept. 2005. doi: 10.1086/432028.

R. B. Tully and J. R. Fisher. Reprint of 1977A&A....54..661T. A new method of determining distance to galaxies. , 500:105–117, Feb. 1977.

A. van der Wel, M. Franx, P. G. van Dokkum, R. E. Skelton, I. G. Momcheva, K. E. Whitaker, G. B. Brammer, E. F. Bell, H. W. Rix, S. Wuyts, H. C. Ferguson, B. P. Holden, G. Barro, A. M. Koekemoer, Y.-Y. Chang, E. J. McGrath, B. Häussler, A. Dekel, P. Behroozi, M. Fumagalli, J. Leja, B. F. Lundgren, M. V. Maseda, E. J. Nelson, D. A. Wake, S. G. Patel, I. Labbé, S. M. Faber, N. A. Grogin, and D. D. Kocevski. 3D-HST+CANDELS: The Evolution of the Galaxy Size-Mass Distribution since z = 3. , 788(1):28, June 2014. doi: 10.1088/0004-637X/788/1/28.

P. G. van Dokkum, K. E. Whitaker, G. Brammer, M. Franx, M. Kriek, I. Labbé, D. Marchesini, R. Quadri, R. Bezanson, G. D. Illingworth, A. Muzzin, G. Rudnick, T. Tal, and D. Wake. The Growth of Massive Galaxies Since z = 2. , 709(2):1018–1041, Feb. 2010. doi: 10.1088/0004-637X/709/2/1018.

P. G. van Dokkum, E. J. Nelson, M. Franx, P. Oesch, I. Momcheva, G. Brammer, N. M. Förster Schreiber, R. E. Skelton, K. E. Whitaker, A. van der Wel, R. Bezanson, M. Fumagalli, G. D. Illingworth, M. Kriek, J. Leja, and S. Wuyts. Forming Compact Massive Galaxies. , 813(1):23, Nov. 2015. doi: 10.1088/0004-637X/813/1/23.

S. D. M. White and M. J. Rees. Core condensation in heavy halos: a two-stage theory for galaxy formation and clustering. , 183:341–358, May 1978. doi: 10.1093/mnras/183.3.341.

D. J. Wilman, M. Fossati, J. T. Mendel, R. Saglia, E. Wisnioski, S. Wuyts, N. Förster Schreiber, A. Beifiori, R. Bender, S. Belli, H. Übler, P. Lang, J. C. C. Chan, R. L. Davies, E. J. Nelson, R. Genzel, L. J. Tacconi, A. Galametz, R. I. Davies, D. Lutz, S. Price, A. Burkert, K.-i. Tadaki, R. Herrera-Camus, G. Brammer, I. Momcheva, and P. van Dokkum. The Regulation of Galaxy Growth along the Size-Mass Relation by Star Formation, as Traced by Hα in KMOS^{3D} Galaxies at $0.7 \lesssim z \lesssim 2.7$. , 892(1):1, Mar. 2020. doi: 10.3847/1538-4357/ab7914.

E. Wisnioski, N. M. Förster Schreiber, S. Wuyts, E. Wuyts, K. Bandara, D. Wilman, R. Genzel, R. Bender, R. Davies, M. Fossati, P. Lang, J. T. Mendel, A. Beifiori, G. Brammer, J. Chan, M. Fabricius, Y. Fudamoto, S. Kulkarni, J. Kurk, D. Lutz, E. J. Nelson, I. Momcheva, D. Rosario, R. Saglia, S. Seitz, L. J. Tacconi, and P. G. van Dokkum. The KMOS^{3D} Survey: Design, First Results, and the Evolution of Galaxy Kinematics from 0.7 <= z <= 2.7. , 799(2):209, Feb. 2015. doi: 10.1088/0004-637X/799/2/209.

E. Wisnioski, N. M. Förster Schreiber, M. Fossati, J. T. Mendel, D. Wilman, R. Genzel, R. Bender, S. Wuyts, R. L. Davies, H. Übler, K. Bandara, A. Beifiori, S. Belli, G. Brammer, J. Chan, R. I. Davies, M. Fabricius, A. Galametz, P. Lang, D. Lutz, E. J. Nelson, I. Momcheva, S. Price,

D. Rosario, R. Saglia, S. Seitz, T. Shimizu, L. J. Tacconi, K. Tadaki, P. G. van Dokkum, and E. Wuyts. The KMOS^{3D} Survey: Data Release and Final Survey Paper. , 886(2):124, Dec. 2019. doi: 10.3847/1538-4357/ab4db8.

S. Wuyts, N. M. Förster Schreiber, D. Lutz, R. Nordon, S. Berta, B. Altieri, P. Andreani, H. Aussel, A. Bongiovanni, J. Cepa, A. Cimatti, E. Daddi, D. Elbaz, R. Genzel, A. M. Koekemoer, B. Magnelli, R. Maiolino, E. J. McGrath, A. Pérez García, A. Poglitsch, P. Popesso, F. Pozzi, M. Sanchez-Portal, E. Sturm, L. Tacconi, and I. Valtchanov. On Star Formation Rates and Star Formation Histories of Galaxies Out to z $\sim$3. , 738(1):106, Sept. 2011. doi: 10.1088/0004-637X/738/1/106.

Appendices

Appendix A

Uncertainties

name	ν_M	$\sigma(\nu_M)$	ν_M^+	$\sigma(\nu_M^+)$	ν_M^-	$\sigma(\nu_M^-)$	ν_R	$\sigma(\nu_R)$	ν_R^+	$\sigma(\nu_R^+)$	ν_R^-	$\sigma(\nu_R^-)$
C-HiZ_z1_195	129.14	5.15	131.16	5.62	126.76	4.80	21.41	6.86	31.11	6.54	11.64	7.26
C-HiZ_z1_258	40.54	1.80	42.11	2.04	38.81	1.58	11.28	1.63	12.05	1.47	10.38	1.82
C-zcos_z1_202	96.97	3.23	98.41	3.39	95.46	3.08	46.69	3.43	48.67	3.30	44.65	3.58
C-zcos_z1_692	59.75	2.35	61.16	2.56	58.19	2.16	16.41	2.66	18.31	2.51	14.43	2.83
E-zmus_z1_119	73.93	4.27	75.11	4.59	72.61	3.98	10.47	5.48	13.16	5.25	7.72	5.73
E-zmus_z1_125	78.67	3.94	79.31	3.93	77.88	4.01	-20.12	6.20	-15.62	6.18	-24.58	6.26
E-zmus_z1_129	91.26	5.82	90.18	6.10	92.12	5.58	-39.70	8.90	-34.36	8.72	-45.11	9.09
E-zmus_z1_166	115.06	4.94	116.18	5.09	114.01	4.82	38.92	7.29	42.50	7.20	35.43	7.40
E-zmus_z1_21	26.16	0.79	27.26	0.87	25.03	0.72	10.52	0.80	10.73	0.74	10.29	0.86

Table A.1: Specific mass and radial growth rates and uncertainties, inferred from best-fit model calculated with R_s, with $R_s + \sigma(R_s)$ (plus symbols in header of table) and with $R_s - \sigma(R_s)$ (minus symbols in header of table). All values have units of 10^{-2} Gyr^{-1}.